The Astrophysical Journal, 798:104 (18pp), 2015 January 10 doi:10.1088/0004-637X/798/2/104
© 2015. The American Astronomical Society. All rights reserved.

THE YOUNG STELLAR OBJECT POPULATION IN THE VELA-D MOLECULAR CLOUD

F. Strafella[1], D. Lorenzetti[2], T. Giannini[2], D. Elia[3], Y. Maruccia[1], B. Maiolo[1], F. Massi[4], L. Olmi[4], S. Molinari[3], and S. Pezzuto[3]
[1] Dipartimento di Matematica e Fisica, Università del Salento, I-73100 Lecce, Italy; francesco.strafella@le.infn.it
[2] INAF-Osservatorio Astronomico di Roma, Via Frascati 33, I-00040 Monte Porzio, Italy
[3] INAF-IAPS, Via Fosso del Cavaliere 100, I-00133 Roma, Italy
[4] INAF-Osservatorio di Arcetri, Largo E. Fermi 5, I-50125 Firenze, Italy
Received 2014 May 26; accepted 2014 October 31; published 2015 January 6

ABSTRACT

We investigate the young stellar population in the Vela Molecular Ridge, Cloud-D, a star-forming region observed by both the *Spitzer*/NASA and *Herschel*/ESA space telescopes. The point-source, band-merged, *Spitzer*-IRAC catalog complemented with MIPS photometry previously obtained is used to search for candidate young stellar objects (YSOs), also including sources detected in less than four IRAC bands. Bona fide YSOs are selected by using appropriate color–color and color–magnitude criteria aimed at excluding both Galactic and extragalactic contaminants. The derived star formation rate and efficiency are compared with the same quantities characterizing other star-forming clouds. Additional photometric data, spanning from the near-IR to the submillimeter, are used to evaluate both bolometric luminosity and temperature for 33 YSOs located in a region of the cloud observed by both *Spitzer* and *Herschel*. The luminosity–temperature diagram suggests that some of these sources are representative of Class 0 objects with bolometric temperatures below 70 K and luminosities of the order of the solar luminosity. Far-IR observations from the *Herschel*/Hi-GAL key project for a survey of the Galactic plane are also used to obtain a band-merged photometric catalog of *Herschel* sources intended to independently search for protostars. We find 122 *Herschel* cores located on the molecular cloud, 30 of which are protostellar and 92 of which are starless. The global protostellar luminosity function is obtained by merging the *Spitzer* and *Herschel* protostars. Considering that 10 protostars are found in both the *Spitzer* and *Herschel* lists, it follows that in the investigated region we find 53 protostars and that the *Spitzer*-selected protostars account for approximately two-thirds of the total.

Key words: catalogs – circumstellar matter – stars: formation – stars: protostars

1. INTRODUCTION

The Vela Molecular Ridge Cloud-D (hereafter VMR-D) ($260^\circ \lesssim \ell \lesssim 264^\circ$; $|b| \lesssim 1^\circ$) is part of a giant molecular complex located along the Galactic plane ($260^\circ \lesssim \ell \lesssim 272^\circ$; $|b| \lesssim 3^\circ$; Murphy & May 1991) and is then well suited to represent a typical star-forming region (SFR) of our Galaxy. For this reason a subregion of this cloud has been the subject of many previous papers, dealing with different observational aspects of the star formation (SF), such as the presence of outflows (Wouterloot & Brand 1999; Elia et al. 2007), jets (Lorenzetti et al. 2002; Giannini et al. 2005, 2013), and clustering (Massi et al. 2000). The continuum submillimeter emission in the VMR-D cloud was surveyed by Massi et al. (2007), who catalogued 29 resolved dust cores and also obtained a further list of 26 unresolved candidate cores. More recently, thanks to the opportunity offered by the *Spitzer Space Telescope*, the VMR-D region was observed with the IRAC ($\lambda = 3.6, 4.5, 5.8, 8.0\,\mu$m) and MIPS ($\lambda = 24, 70\,\mu$m) focal-plane instruments, obtaining in this way six mosaics, covering about 1.2 deg^2, which have been analyzed to produce a merged photometric *Spitzer*-IRAC point-source catalog (hereinafter *Spitzer*-PSC) complemented with MIPS photometry (Strafella et al. 2010, hereinafter Paper I). Further observational progress was made when the BLAST experiment (Pascale et al. 2008) mapped the whole Vela Molecular Ridge in the far-IR (FIR) spectral region ($\lambda = 250, 350, 500\,\mu$m), complementing in this way the *Spitzer* spectral coverage toward long wavelengths. These observations were discussed by Olmi et al. (2009), who obtained a catalog of dense cores/clumps in the VMR-D cloud. The last important observational progress was made with the *Herschel Space Observatory*, which, surveying the Galactic plane in the framework of the Hi-GAL key project, partially mapped the VMR-D region in the FIR spectral range ($\lambda = 70, 160, 250, 350, 500\,\mu$m) with a spatial resolution and sensitivity almost twice that of BLAST. Here we also analyze these observations for the first time, thanks to the support of the Hi-GAL collaboration that provided us with the corresponding calibrated maps. These have been used to extract five single-band photometries that constitute another important spectral extension of our information about this region.

Utilizing these observations, as well as the photometric catalogs made available by the Two Micron All Sky Survey (2MASS) and *Wide-field Infrared Survey Explorer* (*WISE*) all-sky surveys, we have the opportunity to study in much more detail the young stellar objects (YSOs) located in the VMR-D cloud. These objects can be efficiently identified through their infrared colors (see, e.g., Harvey et al. 2007; Gutermuth et al. 2009; Kryukova et al. 2012), which we also exploit here to discriminate genuine YSOs from other contaminant populations of both Galactic and extragalactic origin. All these observational data and tools give us the opportunity to investigate, with unprecedented sensitivity and accuracy, the characteristics of the SF in the VMR-D cloud.

In Paper I, we already considered a subsample of 8796 sources, detected in all four IRAC bands out of the ≈170,000 sources listed in the *Spitzer*-PSC, to carry out a preliminary study of the YSO population in this cloud. Here, to obtain a more complete and accurate view, we revisit our previous preliminary census of the YSOs by including, besides the sources already considered in Paper I, all the other sources detected in at least two out of the four IRAC bands, with the

additional requirement that sources detected in only two bands are also detected in the MIPS 24 μm band.

As in Paper I, we adopt the usual classification of the YSOs based on the near- and mid-IR spectral slope defined as $\alpha = d(\log \lambda F_\lambda)/d(\log \lambda)$, a parameter originally introduced by Lada (1987) to characterize the spectral energy distribution (SED) of these objects that is still largely used and generally interpreted as a proxy of the evolutionary phases experienced by the YSOs. In this scheme, it is customary to distinguish four different classes of YSOs, according to the value of this slope in the $2 \lesssim \lambda(\mu\mathrm{m}) \lesssim 20$ spectral interval: Class I with $\alpha > 0.3$, flat spectrum (FS) for $-0.3 < \alpha < 0.3$, Class II for $-1.6 < \alpha < -0.3$, and finally Class III showing $\alpha < -1.6$. Given the evolutionary significance usually attributed to this parameter (but see also Chen et al. 1995; Young & Evans 2005 for alternative schemes), Class I objects represent an early phase in the evolutionary path of the YSOs toward the zero-age main sequence. Their spectral slope is produced by a central object that already attained its entire initial main-sequence mass but is still surrounded by a remnant infall envelope and possibly an accretion disk. This description naturally implies the existence of an even earlier phase, Class 0 as originally suggested by André et al. (1993), in which the central object is at the end of the free-fall phase but is still increasing its mass by accreting material from a thick surrounding envelope. This fact makes the Class 0 phase difficult to detect in the near-IR and then difficult to classify in the framework of the aforementioned scheme. In this observational classification both Class 0 and Class I are representative of early protostars still surrounded by a remnant infall envelope, although only in the Class 0 stage is the envelope presumed to be more massive than the central object and then opaque to near-IR and possibly also mid-IR wavelengths (both ranges hereinafter referred to as MIR).

To study the SF mechanism in the VMR-D cloud, we proceed along two approaches, both aimed to select candidate protostellar sources by exploiting all the information collected on the continuum emission. The first consists in selecting protostellar candidates by analyzing the *Spitzer* observations through a pipeline based on the criteria used by Harvey et al. (2007) and Gutermuth et al. (2009), which have been proven to be effective in isolating different kinds of possible contaminant sources. In the following, we shall refer to these sources as "*Spitzer* selected," and their analysis will be based on the SEDs assembled by collecting all the available photometries in what we shall call the MIR catalog. The second approach adopts the FIR point of view because it is based on the analysis of the *Herschel* observations, which, being carried out at longer wavelengths, are more sensitive to cold and young protostars. The sources selected in this way will be referred to as "*Herschel* selected," and their SEDs will be arranged in the FIR catalog resulting from the *Herschel* photometry complemented with all the available photometries at shorter and longer wavelengths. Merging the results obtained in these two ways, we expect to obtain a more complete view of the protostellar population in VMR-D, as well as new insights on the SF process in this molecular cloud.

In the following, a brief account of the observational data obtained with *Spitzer* and *Herschel* is given in Section 2, along with a description of the procedures involved in data reduction and photometry. This section also illustrates how we obtain two multiwavelength source catalogs for the VMR-D region: the first, called the MIR catalog, by complementing our previous *Spitzer*-PSC catalog with a set of additional observational data, and the second, the FIR catalog, by assembling the five-band *Herschel* photometry in a single band-merged list of sources.

In Section 3 we select bona fide YSOs out of both catalogs by means of appropriate selection criteria, and in Section 4 we discuss the census and classification of these sources. We also obtain a new estimate of the SF rate and efficiency that is more accurate than that obtained in Paper I based on the sole sources detected in all four IRAC bands.

In Section 5, bolometric temperatures and luminosities are derived for all those sources for which reasonably complete photometric information is available. Here the L_{bol} versus T_{bol} diagram is used to further characterize the YSOs and infer their evolutionary status.

In Section 6 we compare the SF rate and efficiency obtained for VMR-D with those obtained in other SFRs and discuss the global protostellar luminosity function (PLF). For those sources detected by *Herschel* at FIR wavelengths, the envelope mass has been also derived by exploiting a simple modified blackbody model. The luminosity–mass diagram is briefly discussed in the light of the protostellar evolutionary scenario.

Finally, in Section 7, our conclusions are summarized.

2. OBSERVATIONAL DATA

The observational data on the continuum emission of the objects in VMR-D have been collected from many different sources, including existing catalogs, public surveys, and new observations as in the case of the *Herschel* unpublished photometry. Dealing with a conspicuous amount of observational material spread over quite a large spectral interval, we decided to search for candidate YSOs exploiting all the spectral characteristics of their continuum emission. Our approach is twofold and corresponds to adopting an "MIR point of view" and an "FIR point of view" to identify protostellar candidates by means of procedures typically adopted in previous studies of SFRs observed with *Spitzer* and *Herschel*, respectively. In the following, to identify the sky regions involved in the different observations of the VMR-D cloud, we shall refer to Figure 1, which shows the 8 μm IRAC image of the VMR-D cloud overlaid with the contours delimiting the areas observed by different instruments, as well as the contour of the investigated cloud.

2.1. MIR Catalog

We start by considering the sources of the *Spitzer*-PSC catalog covering the region delimited by the cyan polygon in Figure 1. To arrange all of the available continuum observations for easy access and at the same time obtain the SEDs, we generated a new catalog containing the fluxes from all the available photometric surveys of this cloud from the near-IR to the submillimeter spectral range. This catalog is essentially a spectral extension of our previous *Spitzer*-PSC catalog and contains, besides the *Spitzer*-IRAC/MIPS (3.6, 4.5, 5.8, 8.0, 24, 70 μm) photometry, also 2MASS (J, H, K bands), *WISE* (3.4, 4.6, 12, and 22 μm), *Herschel* (70, 160, 250, 350, and 500 μm), and SEST-SIMBA (1200 μm) observations.

Given the heterogeneous nature of the observational data, we adopted specific criteria in associating with the same source fluxes obtained at different wavelengths and with different spatial resolutions. This is a typical problem in assembling information coming from different catalogs, and it is usually mitigated by requiring that the distance between the centroids

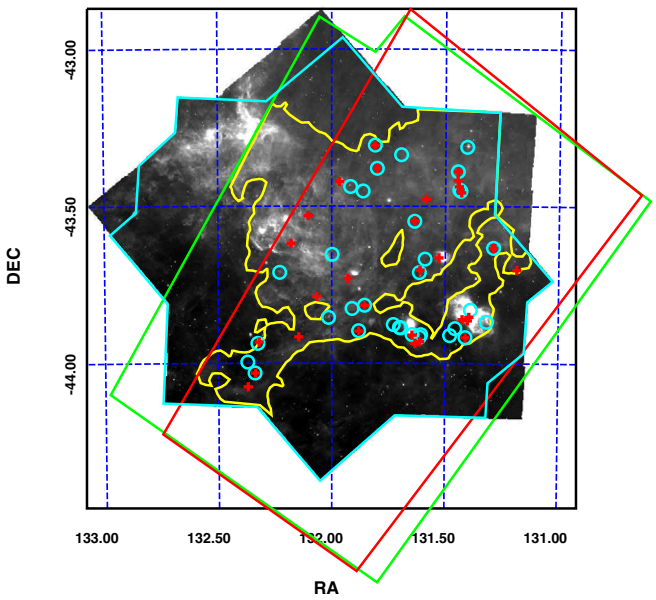

Figure 1. IRAC 8.0 μm image of the VMR-D investigated field with the positions of the *Spitzer* (cyan circles) and *Herschel* (red crosses) protostellar sources located ON-cloud and in the common area surveyed by both *Spitzer* and *Herschel*. The cyan polygon delimits the coverage of the *Spitzer*-PSC catalog (Paper I), while the large tilted trapezoids delimit the coverage of the *Herschel* SPIRE (green) and PACS (red) Hi-GAL observations analyzed in this work. The yellow contour line corresponds to a column density $N(H_2) = 6.5 \times 10^{21}$ cm^{-2} and delimits the region we consider ON-cloud (see text). For a normal interstellar extinction curve this corresponds to $A_V \sim 3.5$ mag.

of the sources to be associated is smaller than a predetermined value depending on the spatial resolution of the specific catalogs. This is also our approach even if more complex association procedures could be devised, involving further considerations of the flux values to be associated and, in turn, of the possible underlying spectral shapes (see, e.g., Roseboom et al. 2009; Budavari & Szalay 2008). In our case we prefer to consider the positional uncertainty, instead of the beam size, as a measure of the spatial accuracy of a given catalog because it is usually evaluated after an accurate statistical analysis and is generally more conservative. In this way we minimize possible mismatches in associating with the same source the fluxes from different catalogs, especially in crowded regions, even if we risk missing some source association.

Our procedure adopts the fiducial positions of the sources reported in the *Spitzer*-PSC catalog that are used to find possible counterparts at other wavelengths. In this way, the other catalogs are considered as ancillary. The final product is a catalog containing the same number of entries as the *Spitzer*-PSC, but complemented with the associated fluxes observed at different wavelengths. In Table 1 we report the association radii adopted for the catalogs considered in this work, along with the associated beam sizes, completeness fluxes, and relevant references.

In practice, we consider as acceptable the associations for which the distance $\Delta\theta$ between the position of the *Spitzer*-PSC source and the position of a source in a given catalog is less than the sum of the corresponding uncertainties, namely, $\Delta\theta < \delta\theta_{\rm PSC} + \delta\theta_{\rm cat}$. In the case of multiple associations we always adopt the nearest source to the fiducial *Spitzer*-PSC position, allowing, however, that multiple *Spitzer*-PSC sources could be similarly associated with the same object of another catalog, a problem that will be taken into account later in the analysis. After scanning all the considered catalogs for positional association with the *Spitzer*-PSC sources, we obtained a set of corresponding fluxes that, once assembled, constitute the MIR multiwavelength catalog of our interest.

2.2. FIR Catalog

The VMR-D cloud is located across the Galactic plane and has been partially mapped by *Herschel* during the completion of the Hi-GAL key project for an FIR survey of the Galactic plane (Molinari et al. 2010). As is shown in Figure 1, the survey coverage is incomplete because at these longitudes the observing strategy of the Hi-GAL survey preferred to follow the warp of the Galaxy instead of the Galactic plane. The VMR-D cloud has also been mapped by the BLAST experiment at 250, 350, and 500 μm, albeit with a significantly lower spatial resolution and sensitivity. Because of this, in the following we prefer to use the *Herschel* observations instead of the BLAST ones, alleviating in this way the problems related to both the strong and variable background and the source confusion.

Thanks to the Hi-GAL consortium, we obtained calibrated maps (Bernard et al. 2000) of our region in which the artifacts introduced by the map-making technique have been removed or heavily attenuated by means of a weighted post-processing of the maps themselves (Piazzo et al. 2012). The source detection and photometry have been carried out on these maps by using the CuTeX package (Molinari et al. 2011), a software specifically designed to detect and extract compact sources against a strong and variable background. In this way we obtained five lists of sources, corresponding to the five bands of the Hi-GAL survey, which have been merged adopting the association radii reported in Table 1 for the *Herschel* photometry. In assembling this catalog, the merging process proceeded from long to short wavelengths, updating the position of each merged source with the coordinates corresponding to the source actually associated with the shortest wavelength, with the aim of retaining the position associated with the shortest detected wavelength.

Subsequently, to evaluate accurate bolometric quantities, we also extended the spectral information on these FIR sources by complementing the merged *Herschel* catalog with *Spitzer* and *WISE* fluxes, at shorter wavelenths, and with 1.2 mm SIMBA fluxes (Massi et al. 2007), at longer wavelengths. In doing this, we always adopt the positional requirements reported in Table 1 to associate complementary fluxes with the fiducial positions in the multiband catalog of the *Herschel* sources.

As for the previous MIR catalog, the merging procedure allows the possibility of multiple source associations, within the constraints in Table 1, a problem that will be taken into account in the subsequent analysis of this FIR catalog.

3. SOURCES SELECTION

To obtain a census as complete as possible of the protostellar content in the VMR-D cloud, we exploit both the MIR and FIR catalogs based on the *Spitzer* and *Herschel* observations, respectively. Because in the following analysis we select candidate protostars from these catalogs, here we separately illustrate the selection procedure and the classification criteria adopted to characterize the selected sources.

3.1. MIR Sources

A preliminary analysis, limited to the *Spitzer* sources detected in all four IRAC bands, was already presented in Paper I. Here we enlarge the database to all the sources detected with

Table 1
Catalogs Considered

Name	2MASS	*WISE*	*Spitzer*-IRAC+MIPS	*Herschel*	SEST-SIMBA
Band	*JHK*	3.4 4.6 12 22	3.6 4.5 5.8 8.0 24 70	70 160 250 350 500	1200
Beam size (″)	2.5–3	6–12	1.7–6	7.6 12.3 18 25 36	24
Association radius[a] (″)	0.6	0.9	1	4 8 11 16 21	12
Completeness[b] flux (mJy)	0.76 1.23 1.67	4.9 2.7 3.2 5.3	0.05 0.05 0.29 0.4 2.0 500	1800 1100 600 600 600	20
Reference[c]	1	2	3	4	5

Notes.
[a] 1σ positional uncertainty for 2MASS and *WISE* catalogs. For *Spitzer*, *Herschel*, and SEST data the association radius is estimated from the references given.
[b] Completeness fluxes are meant for crowded regions: 2MASS, 99%; *WISE*, 95%; *Spitzer*, 99%; *Herschel*, 90%; SEST, sensitivity limit.
[c] References: (1) Skrutskie et al. 2006; (2) Cutri et al. 2013; (3) Paper I; (4) Elia et al. 2013; (5) Massi et al. 2007.

Table 2
Spitzer Source Counts through the Selection Pipeline

Step	1234[a]	123X	12X4	1X34	X234	XX34	1XX4	12XX	1X3X	X2X4	Total
0: first selection[b]	8852(436)	7210(28)	151(12)	19(12)	30(19)	9(9)	1(1)	116(116)	2(2)	1(1)	16391
1: reddened stars	−6110	−6063	−9	−10	−15	−6	0	−3	0	−1	−12217
2: Har07 criteria[c]	−2059	0	−142	0	−15	0	−1	0	0	0	−2217
3: Gut09 criteria[d]	−17	−467	0	0	0	0	0	0	0	0	−484
4: undefined slope	−9	−3	0	0	0	0	0	0	0	0	−12
Total	657	677	0	9	0	3	0	113	2	0	1461[e]

Notes.
[a] Four digits are used to refer to the IRAC bands in which the sources have been detected: e.g., 12XX refers to sources detected in the first and second band only. The X23X column is not reported because no sources of this kind have been found.
[b] Numbers in parentheses are sources showing also MIPS 24 μm fluxes.
[c] Harvey et al. (2007).
[d] Gutermuth et al. (2009).
[e] Nine bright 24 μm sources, detected in only one IRAC band, have been subsequently added (see text).

photometric uncertainties $\sigma < 0.2$ mag in at least three out of the four IRAC bands, augmented with those sources that, detected only in two IRAC bands, are also detected in the MIPS 24 μm band. As a final addition, with the aim of considering potentially interesting objects, we also include a few special cases that, detected in only one IRAC band, are particularly bright at $\lambda = 24$ μm and show a spectral slope that is compatible with a Class I SED.

While including sources detected in only three wavelengths helps mitigate possible selection effects due to different sensitivities in the IRAC bands, considering also objects detected in only two IRAC bands and in the MIPS 24 μm band allows us to include further sources that, for different reasons, could appear faint in particular wavelengths, such as transition disks with large inner holes or unusual circumstellar geometries that could escape detection in some IRAC bands. The last addition of sources detected only in one IRAC band aims to include potentially interesting sources that could represent deeply embedded objects barely visible in the IRAC bands or even Class II sources with inner disks cleared from dust.

In this way we extracted a total number of 16,391 sources, whose distribution in the different typologies is shown in the first row of Table 2. These constitute the working database in which we search for candidate YSOs by using specific selection criteria aimed at excluding both Galactic and extragalactic contaminants.

3.1.1. Selection Phase

The first obvious step in selecting bona fide YSOs is to exclude from further investigation all those sources that could be interpreted as reddened stellar photospheres. To this aim, following Harvey et al. (2006), we compared the observed with the model fluxes, based on the stellar photosphere Kurucz–Lejeune models, taken from the Spitzer Science Center's Star-Pet tool.[5] These fluxes are given just as they would be observed in the IRAC and MIPS bands and are then directly comparable with our observational data. In this respect, we scrutinized all the sources with at least three detections in the $2.2 \leqslant \lambda \leqslant 24$ μm spectral region, and, considering the effects of the extinction law given by Flaherty et al. (2007), we found 12,217 sources that can be reasonably fitted with a reduced $\chi^2 < 2.5$ and then represent, most probably, reddened photospheres that have been consequently excluded from further consideration. With this choice the probability that some reddened normal star still contaminates our sample despite this filtering is less than ∼10%, a risk that will be further mitigated by the subsequent selection steps. In Figure 2 we show the distribution of the parameters involved in this procedure, noting that the bulk of the sources excluded by the adopted cut in χ^2 involves essentially objects with slopes $-3.5 \lesssim \alpha \lesssim -1.5$ (bottom right panel).

After this preliminary step (Step 1 in Table 2), we are left with 4174 sources that have been further filtered adopting the selection criteria used by Harvey et al. (2007, see their Table 1) to identify extragalactic contaminants on the basis of the 4.5, 8.0, and 24 μm photometry. In this phase we also discarded sources with both color [4.5]-[8.0] < 0.7 and spectral slope $\alpha < -1.6$ as representing normal background stars remaining even after the previous dereddening phase and visible in Figure 3 as a cloud of small black points. Applying these criteria to our sample,

[5] http://ssc.spitzer.caltech.edu/warmmission/propkit/pet/starpet/index.html

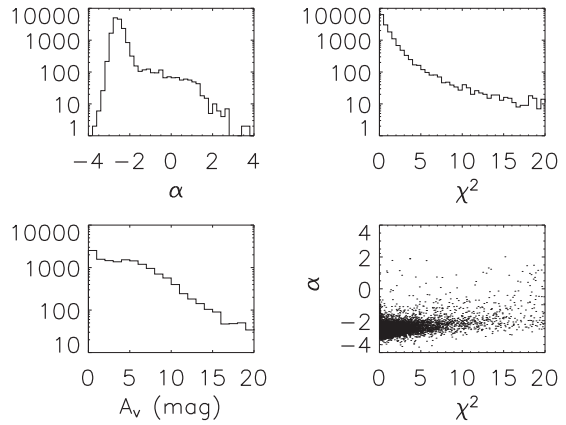

Figure 2. Best-fit parameters obtained after comparing the observed MIR SEDs with the reddened photospheric emission models (see text). Upper panels: distribution of the spectral slopes α (left) and the reduced χ^2 values (right) obtained by fitting the SEDs. Lower panels: distribution of the visual extinctions A_V corresponding to the best fits (left) and the α vs. χ^2 scatter plot (right).

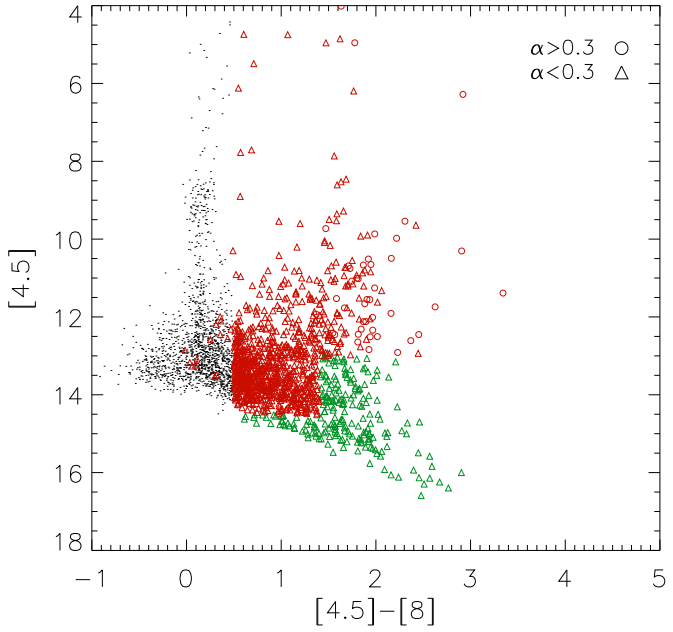

Figure 3. IRAC color–magnitude diagram [4.5] vs. [4.5]−[5.8] showing the position of different objects. Points represent background stars; triangles and circles are objects with $\alpha < 0.3$ and $\alpha > 0.3$, respectively. Green and red symbols indicate objects that are rejected and passed, respectively, after applying the Harvey et al. (2007) criteria (see text).

we eliminate 2217 sources whose different typologies are reported in the row labeled "Step 2" in Table 2.

Excluding also these objects, we count 1957 sources that have been further scrutinized with additional color–color and color–magnitude criteria similar to those devised by Gutermuth et al. (2009, their Appendix A) to identify, and then exclude, further extragalactic and Galactic contaminants. Following these authors, our sources have been examined in three different phases, the first consisting in the identification of sources whose colors are compatible with polycyclic aromatic hydrocarbon (PAH) contaminated galactic and extragalactic sources, active galactic nuclei, and protostellar shocks. In this phase 484 sources (Step 3 row in Table 2) were flagged as contaminants so that, excluding them from further consideration, 1473 sources remain. In Figure 4 the [3.6]−[4.5] versus [4.5]−[5.8] diagram

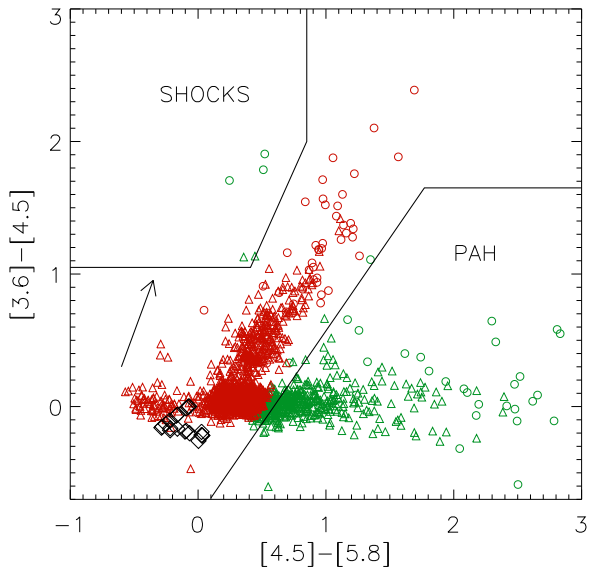

Figure 4. Color–color diagram exploiting IRAC fluxes to select candidate YSOs according to the Gutermuth et al. (2009) criteria. The reddening vector is also shown, corresponding to a visual extinction $A_V = 50$ mag and to the reddening law determined by Flaherty et al. (2007). Symbols are as in Figure 3, except the black diamonds in the lower left corner, which represent the locus of the stellar photospheres.

is shown with the two regions, delimited by the solid line, corresponding to the colors appropriate for shocks (upper left) and PAH-contaminated (lower right) sources (see also Gutermuth et al. 2009, Figure 15).

As in the second phase of Gutermuth et al. (2009, Appendix A), to include possible YSOs detected only in the [3.6] and [4.5] bands but not at 24 μm, we reconsidered the whole catalog to select all the cases with fluxes in *JHK* [3.6] and [4.5] bands, but requiring a photometric uncertainty $\sigma < 0.1$ mag in the *JHK* bands to minimize chances of picking up sources only because of the additional uncertainty implied by the dereddening procedure at these shorter wavelengths. In this way we selected 48 sources that, however, do not satisfy the phase 2 criteria of Gutermuth et al. (2009, Appendix A) and thus leave unaffected the total number of candidate YSOs.

In the third phase we recovered sources that, although detected in only one IRAC band, are bright at 24 μm. These are potentially interesting sources because they could represent deeply embedded objects barely visible in the IRAC bands or even Class II sources with inner disks cleared from dust. Because of this, we include in our sample of candidate YSOs all the sources with bright MIPS 24 μm photometry ([24] < 7), to mitigate extragalactic contamination, and color $[X] - [24]$ greater than the corresponding color expected for an SED with slope $\alpha = -0.3$, namely, $[X]-[24] > 5.43, 4.77, 4.10$, and 3.22 for the four bands, where $[X]$ is the only available IRAC band photometry. In this way we recovered 4, 4, 0, and 1 sources with good photometry in the IRAC 3.6, 4.5, 5.8, and 8.0 μm bands, respectively, increasing to 1482 the total number of candidate YSOs. All of these nine additional sources also show good MIPS 24 μm photometry with $\sigma < 0.2$ mag. Finally, we complete the selection by excluding 12 sources showing a particularly irregular SED that cannot be represented by a single slope (see Table 2 and Section 4.1), suggesting that they are the result of source confusion. The final list of candidate YSOs selected out of the *Spitzer*-PSC catalog is then composed of 1470 sources.

3.2. FIR Sources

Another starting point to select candidate protostellar sources in the VMR-D cloud can be adopted by using the *Herschel* observations, which, arranged in an FIR catalog of compact sources as described in Section 2.2, can be exploited to analyze the SEDs. In this respect our approach to selecting candidate protostars is quite different because at FIR wavelengths the observations are more sensitive to colder objects, complementing in this way our view of the SF process.

Basically, candidate sources are selected by adopting specific prescriptions (see also Giannini et al. 2012) aimed at excluding cases that, also owing to confusion problems, appear as spectrally inconsistent. To this aim, we first eliminate from our FIR catalog the ambiguities due to the presence of multiple associations, retaining only the nearest one to the fiducial catalog position, namely, that determined in the band-merging phase (see Section 2.2). Then, to prepare the analysis of the SEDs, we select the sources detected in at least three out of the four *Herschel* bands at $\lambda \geqslant 160$ μm, not peaking at 500 μm, and without a dip between three adjacent wavelengths. In addition, we also require that these sources appear as resolved at $\lambda_{\rm ref} = 250$ μm, a reference wavelength we assume to correspond to an optically thin regime (Elia et al. 2013). All of these prescriptions are in view of exploiting a simple modified blackbody model to fit the *Herschel* FIR fluxes in the subsequent classification phase.

The SEDs selected in this way have, in fact, been fitted with a simple modified blackbody model that assumes an optically thin regime for wavelengths $\lambda > \lambda_0$ and an optical depth described by $\tau = (\nu/\nu_0)^\beta$, where $\beta = 2$ is appropriate for simple dust models and $\nu_0 = c/\lambda_0$ is the frequency corresponding to $\tau = 1$. The model fluxes are computed from the relation

$$F_\nu = (1 - e^{-\tau_\nu}) B_\nu(T_d)\Omega, \quad (1)$$

where T_d is the dust temperature and Ω is the solid angle subtended by the source to the observer. The fact that Ω can be observationally constrained clarifies our previous requirement for resolved sources so that, to this aim, we consider as spatially resolved all the sources with a deconvolved size satisfying

$$\mathrm{FWHM}_{\lambda,\mathrm{dec}} = \sqrt{\mathrm{FWHM}_\lambda^2 - \mathrm{HPBW}_\lambda^2} > 0.6 \times \mathrm{HPBW}_\lambda, \quad (2)$$

where FWHM_λ is the observed source size and HPBW_λ is the instrumental half-power beam width at the given wavelength. With these choices, and assuming a VMR-D distance of 700 pc (Liseau et al. 1992), the beam size and the minimum resolved size correspond to ~0.06 pc and ~0.02 pc, respectively.

However, constraining Ω with the deconvolved size at $\lambda_{\rm ref} = 250$ μm is not strictly appropriate at all wavelengths, owing to the increase of the apparent size when colder and larger volumes become "visible" at longer wavelengths. For this reason, before applying the fitting procedure, we normalized the fluxes obtained at longer wavelengths to the same angular size by scaling them with respect to the ratio of the deconvolved sizes, namely, $\mathrm{FWHM}_{\lambda_{\rm ref},\mathrm{dec}}/\mathrm{FWHM}_{\lambda,\mathrm{dec}}$. This treatment is justified by the expectation that the radial density law in the cores is of the kind $\rho(r) \propto r^{-2}$, implying for the mass that M(r)$\propto r$ (Shu 1977), a situation that, in the absence of a strong temperature gradient, suggests the aforementioned flux scaling at optically thin wavelengths (Motte & André 2001; Giannini et al. 2012).

Finally, by using a fitting procedure based on the Levenberg–Marquardt technique (Markwardt 2009), we derive best-fitting values for T_d and λ_0, in this way also checking that the best fits always occur for $\lambda_0 < 100$ μm, a posteriori justifying our assumption of an optically thin regime at $\lambda = 250$ μm.

4. CLASSIFICATION

Here we exploit the fluxes collected in both the MIR and the FIR catalogs to classify the protostars and characterize the SF process in the VMR-D cloud. In the following we discuss two different schemes we use for classifying *Spitzer* and *Herschel* selected sources, respectively.

4.1. MIR Sources

As described in the introduction, here we adopt the YSO classification scheme based on the spectral slope as evaluated in the MIR spectral range, with the addition of a further class, Class 0. The latter has been introduced to include objects in the earliest phases that are very faint or even undetected in the MIR, being more easily detected in the FIR/submillimetric range. The physical basis for this scheme relies on the evolutionary scenario in which a central object is initially surrounded by an envelope of gas and dust whose spectral importance decreases with time in favor of an emerging hotter circumstellar disk. The global spectral appearance consequently changes so that an external observer would classify the YSO depending on the MIR spectral slope and then on the elapsed time from the end of the envelope-dominated phase corresponding to the Class 0 stage. However, owing to the intrinsic MIR faintness during the Class 0 stage, the least evolved protostars cannot be efficiently identified in this spectral region, so that other complementary classification schemes have been proposed that are based on different observables, such as the bolometric luminosity and temperature (see Chen et al. 1995; Young & Evans 2005), quantities we shall consider later.

Here we limit ourselves to classifying the candidate YSOs by considering the spectral slope in the interval $2 \lesssim \lambda(\mu\mathrm{m}) \lesssim 24$ and to this aim, we use all the available fluxes collected in the MIR catalog. Two distributions are shown in Figure 5, corresponding to the slopes obtained for the YSOs located ON- and OFF-cloud: 869 and 356 cases, respectively. Hereinafter with ON-cloud sources we mean those projected within the yellow contour line shown in Figure 1, corresponding to $N(\mathrm{H_2}) = 6.5 \times 10^{21}$ cm^{-2} in the column density map obtained by exploiting the *Herschel*/Hi-GAL observations with the same procedure adopted by Elia et al. (2013). After regridding the 160, 250, and 350 μm maps onto the pixels of the 500 μm map, we computed the corresponding cold dust temperature and column density maps. This has been done by fitting the modified blackbody model in Equation (1) to the intensities observed at the different wavelengths in each pixel of our maps, assuming the optically thin case as a justified approximation at these wavelengths. Note, however, that in the region outside the *Herchel*-PACS coverage only the three SPIRE fluxes are available, and thus here we derive less accurate column density values.

The final contour line obtained, beyond delimiting the cloud that is visible on our maps, corresponds to a visual extinction of $A_V \sim 3.5$ that is approximately the extinction beyond which the largest number of protostars is found in the Orion A molecular cloud (Lada et al. 2013) and the column density distribution in the Auriga I cloud enters the low-density region of the cloud itself (Froebrich & Rowles 2010).

Conversely, the OFF-cloud sources, which we consider as representative of the background, are those located outside

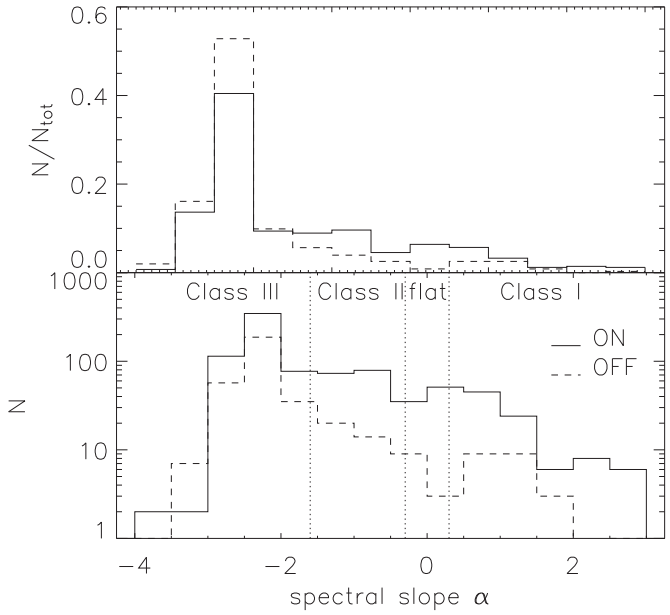

Figure 5. Lower panel: distribution of the MIR spectral slope α for the *Spitzer*-selected candidate YSOs. Sources located ON-cloud (solid line) and OFF-cloud (dashed line) are shown separately. The distinction refers to the position of the sources with respect to the contour line corresponding to 6.5×10^{21} cm^{-2} in the column density map obtained by the *Herschel* observations (see text and Figure 1). In the upper panel the same distributions are shown normalized.

Table 3
VMR-D Statistics of the *Spitzer* YSOs (MIR Catalog)

Region	ON[a]	OFF[a]	OUT[a]	TOT	ON–OFF[b]
Ω[c](deg^2) →	0.54	0.52	0.14	1.20	0.54
Class I	105 (12%)	22	22	149	82 ± 11 (15%)
Flat spectrum	58 (7%)	6	9	73	52 ± 8 (10%)
Class II	171 (20%)	40	33	244	129 ± 14 (24%)
Class III	535 (61%)	288	181	1004	236 ± 28 (51%)

Notes.
[a] The columns ON and OFF refer to regions inside and outside, respectively, the column density contour line derived from the *Herschel* observations and shown in Figure 1. The OUT column refers to sources of the IRAC catalog outside the coverage of the *Herschel*-SPIRE observations.
[b] The difference has been weighted by the corresponding solid angles, and the estimated uncertainty is Poissonian.
[c] Solid angle subtended by the different subregions.

the previous contour line. Our cloud is embedded in a larger complex so that what we define as background here could not represent the true Galactic background, but instead should be considered a mixture of two components, one associated with the same Vela cloud and the other with the field. Despite this ambiguity, the subtraction of the OFF- from the ON-cloud component, weighting for the corresponding solid angles, remains appropriate to estimate the consistency of the "genuine" ON-cloud population.

The two histograms in Figure 5 show that earlier classes are relatively more abundant in the ON-cloud region and simply reflect the statistics, obtained for the different classes at the end of the source classification phase, which is reported in Table 3. In this respect it is worth noting that the counts in Table 3 do not change significantly by moving the boundary line of the ON-cloud region up to ∼15% in column density.

In this analysis we also discarded 12 sources, reported in Table 2 as Step 4 of the selection pipeline, because their SED

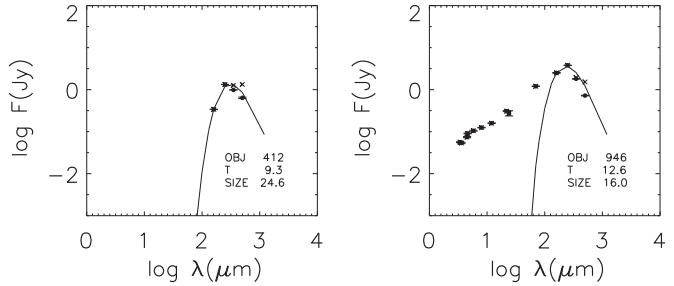

Figure 6. Examples of SED fits obtained with a modified blackbody model for a typical starless (left) and protostellar (right) source. The deconvolved size at 250 μm (in arcsec) and the best-fit temperature are also indicated.

is probably affected by confusion problems. For these sources the linear fit in the $\log(\lambda F_\lambda)$ versus $\log(\lambda)$ diagram could not reasonably account for their peculiar SED that appears to be monotonically decreasing up to 8 μm, reminiscent of a Class III, and then suddenly rising in the 24 μm band.

We note, however, that despite our efforts in eliminating the background contamination, the number of Class III sources remains the most uncertain because the colors of the normal stars closely mimic those of this class. Consequently, the number of the Class III sources should be considered more as an upper limit than as an intrinsic characteristic of the cloud.

4.2. FIR Sources

Our FIR catalog is based on the *Herschel* sources, and thus it is expected to be particularly rich in cold objects. In principle, such objects can be either early protostars or quiescent cores, and hence it is essential to devise some criterion to distinguish protostellar from starless cores. This task can be accomplished by considering that while starless cores should be characterized by a single cloud temperature, the protostellar ones are instead expected to show a temperature gradient just because they harbor a protostar. To this aim, we use the modified blackbody model described by Equation (1) to fit the FIR spectral points, but excluding the 70 μm fluxes since at this short wavelength the emission more likely results from warmer material and is then useful to trace the early protostellar phases. In other words, the observed 70 μm flux is taken as discriminating the protostellar/starless nature of the sources depending on its compatibility with the flux expected from the model that best fits the SED at the longer wavelengths. Consequently, objects showing a 70 μm flux exceeding the model flux by more than 3σ are considered protostars, while in all the other cases, including those without a 70 μm detection, we simply classify the sources as starless. In this phase, to allow a reasonable fit of the SED at $\lambda > 70$ μm, we only consider *Herschel* sources showing at least three detections in the $160 \leqslant \lambda \leqslant 500$ μm spectral range.

This classification procedure is illustrated in Figure 6, where two typical fits obtained with the model in Equation (1) are shown. In both cases we obtain a reasonable fit at $\lambda > 160$ μm, but in the right panel the 70 μm flux is clearly in excess with respect to that expected on the basis of the model. Interpreting this as a signature for the presence of a hotter embedded source, we classify this object as a candidate protostar. The converse is valid for the left panel, showing a source we classify as starless.

In this way we identified 31 protostellar and 100 starless sources in the overlap region covered by both *Herschel* and *Spitzer* observations (see Figure 1) that reduce to 30 and 92 objects, respectively, when we consider only those located in the ON-cloud region. Their positions are shown in Figure 1 as red crosses, superimposed on the *Spitzer* 8 μm map of the VMR-D

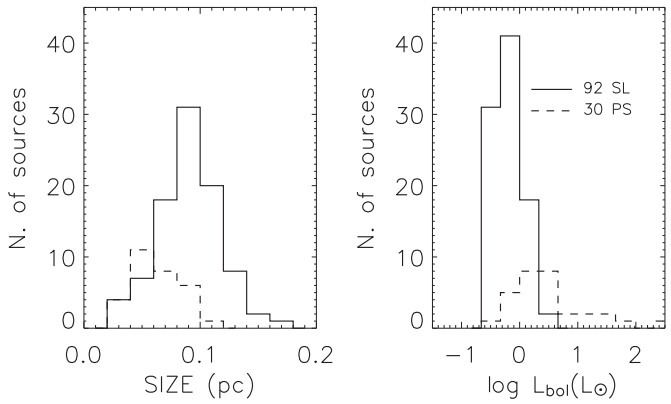

Figure 7. Distribution in size (left) and luminosity (right) obtained for protostellar (dashed) and starless (continuous) sources detected ON-cloud by *Herschel*.

region, and their distribution in sizes is shown in the left panel of Figure 7. The latter values are derived by using the deconvolved angular sizes observed at 250 μm and assuming a distance of 700 pc. Note that because we need to consider the 70 μm flux to discriminate protostars, all these objects are confined to the region also covered by *Herschel*-PACS observations. In Table 4 we summarize the results of this classification by exploiting the bolometric temperature, introduced in the next section, as an alternative parameter to subdivide the *Herschel* protostars in classes.

5. BOLOMETRIC QUANTITIES

Motivated by the difficulties in classifying protostars relying on either the MIR (Lada 1987) or the submillimeter (André et al. 1993) spectral range, Chen et al. (1995) introduced a model-independent classification scheme based on the bolometric luminosity and the so-called bolometric temperature, originally defined by Myers & Ladd (1993). Because these two quantities can be derived observationally by using all the available fluxes, the resulting classification scheme is independent of the spectral characteristics in a predefined spectral range, so that all the evolutionary phases, including Class 0, can be more naturally included. The drawback is that bolometric quantities are more difficult to estimate because their accuracy depends on the observational coverage of the SED, particularly in the spectral region where most of the object's luminosity is emitted.

In this respect the SEDs of the protostellar sources, especially for the earliest objects, typically peak at wavelengths longer than 24 μm, so that the number of cases in which we can directly estimate the bolometric luminosity is usually limited by the availability of the FIR fluxes. In our case, because the VMR-D observations cover a wide spectral range, we can accurately compute the bolometric luminosity at least for all those sources that have been detected in a large spectral range.

5.1. Spitzer Selected Sources

We compute the bolometric luminosities of the *Spitzer* ON-cloud sources by using the fluxes reported in the MIR catalog, recalling that this also includes the associated *Herschel* fluxes, as described in Section 2.1. Preliminarily, we purge the MIR catalog of multiple associations with counterparts coming from another catalog that satisfy the adopted positional constraint with more than one *Spitzer*-PSC source. In such cases we leave only the nearest association to the *Spitzer*-PSC position, ensuring in this way that each associated flux enters only

Table 4
VMR-D Statistics of the *Herschel* Protostars (FIR Catalog)

Region[a]	ON	OFF
Ω(deg^2) →	0.48	0.33
Class 0[b]	17	···
Class I	12	1
Flat spectrum	1	···

Notes.
[a] ON and OFF have the same meaning as in Table 3, but the corresponding solid angles are further limited by the *Herschel*-PACS coverage (see text).
[b] Based on the correspondence between bolometric temperature and classes (see text and Figure 9).

one of the SEDs we consider. Furthermore, to obtain accurate luminosity values, we limited our attention to considering only the sources satisfying all of these requirements:

1. the SED is composed of at least six observed spectral points;
2. at least two FIR fluxes ($\lambda \geqslant 24$ μm) are available; and
3. at least three fluxes are available in the MIR ($\lambda < 24$ μm) spectral region.

As a consequence, because long-wavelength fluxes are needed to accurately obtain bolometric quantities, we practically focus our attention on the ON-cloud sources falling within the region surveyed by *Herschel* PACS+SPIRE, as is shown in Figure 1. With these criteria we practically select 33 objects whose SEDs are Class I and FS and whose photometry is reported in Table 5. For these we assume a distance of 700 pc (Liseau et al. 1992) to obtain the luminosity $L_{\rm bol}$ that is computed by using a power-law piecewise integration between data points, including a Rayleigh–Jeans tail extending toward the long wavelengths. For the same objects we also compute the bolometric temperature given by (Myers & Ladd 1993):

$$T_{\rm bol} = 1.25 \times 10^{-11} \overline{\nu}, \quad (3)$$

where $\overline{\nu}$ is the mean frequency weighted with respect to the flux, defined as

$$\overline{\nu} = \frac{\int_0^\infty \nu F_\nu d\nu}{\int_0^\infty F_\nu d\nu}. \quad (4)$$

The result of this procedure is presented in Figure 8, where the bolometric luminosities and temperatures, computed for the 33 ON-cloud sources satisfying the preceding criteria, are shown superposed on some evolutionary tracks taken from Myers et al. (1998). In the bottom of this figure we also report the correspondence between $T_{\rm bol}$ and the evolutionary classes suggested by Chen et al. (1995) and Evans et al. (2009). It is noteworthy that the VMR-D cloud shows a relatively large number of sources (7 out of 33) that, classified as Class I (6 sources) and FS (1 source) according to their spectral slope in the MIR spectral range, show however $T_{\rm bol} < 70$ K, suggesting instead that they could well be Class 0 objects as far as the bolometric temperature is concerned. This result confirms that the *Spitzer* sensitivity is sufficient to detect at least some of the Class 0 objects (Dunham et al. 2014), and in fact we find that in the VMR-D region ~20% of the *Spitzer*-selected protostars can well be Class 0 sources.

5.2. Herschel-selected Sources

Herschel observations are more sensitive to the early protostellar phases (see, e.g., Stutz et al. 2013) and thus give us the

Table 5
Photometry of the *Spitzer*-selected Protostars[a]

ID	PSC[b]	R.A.	Decl.	$F_J \pm \Delta F_J$	$F_H \pm \Delta F_H$
$F_K \pm \Delta F_K$	$F_{W1} \pm \Delta F_{W1}$	$F_{W2} \pm \Delta F_{W2}$	$F_{W3} \pm \Delta F_{W3}$	$F_{W4} \pm \Delta F_{W4}$	$F_{3.6} \pm \Delta F_{3.6}$
$F_{4.5} \pm \Delta F_{4.5}$	$F_{5.8} \pm \Delta F_{5.8}$	$F_{8.0} \pm \Delta F_{8.0}$	$F_{24} \pm \Delta F_{24}$	$F_{70} \pm \Delta F_{70}$	$F_{160} \pm \Delta F_{160}$
$F_{250} \pm \Delta F_{250}$	$F_{350} \pm \Delta F_{350}$	$F_{500} \pm \Delta F_{500}$	$F_{1200} \pm \Delta F_{1200}$[c]		
1	8036	131.28840	−43.63255	...	...
...	0.00016 ± 0.00005	0.00025 ± 0.00009	0.0027 ± 0.0003	0.0165 ± 0.0013	0.000040 ± 0.000004
...	...	...	0.017 ± 0.003	...	1.09 ± 0.08
2.70 ± 0.06	3.08 ± 0.08	1.63 ± 0.06	...		
2	10558	131.31710	−43.86800	0.000682 ± 0.000057	0.000835 ± 0.000088
0.00076 ± 0.00010	...	...	...	...	0.00069 ± 0.00003
0.00042 ± 0.00001	...	...	0.0361 ± 0.0053	...	2.71 ± 0.03
...	...	...	...		
3	17534	131.38797	−43.82994	0.051 ± 0.01	0.136 ± 0.004
0.29 ± 0.01	0.82 ± 0.05	0.94 ± 0.04	1.97 ± 0.02	9.01 ± 0.07	0.58 ± 0.02
0.60 ± 0.02	0.68 ± 0.02	1.08 ± 0.02	1.93 ± 0.26	25.5 ± 2.5	...
...	...	32.3 ± 0.1	...		
4	19124	131.40512	−43.31155	0.00099 ± 0.00006	0.0199 ± 0.0005
0.158 ± 0.003	1.44 ± 0.15	4.6 ± 0.7	2.12 ± 0.03	1.36 ± 0.03	1.13 ± 0.05
1.87 ± 0.08	2.44 ± 0.04	2.59 ± 0.07	0.94 ± 0.15	0.49 ± 0.01	...
...	...	...	...		
5	19667	131.41093	−43.91746	...	0.0023 ± 0.0002
0.0089 ± 0.0003	0.0233 ± 0.0005	0.0405 ± 0.0007	0.062 ± 0.001	0.259 ± 0.005	0.0263 ± 0.0007
0.0326 ± 0.0014	0.0419 ± 0.0008	0.050 ± 0.001	0.194 ± 0.008	0.48 ± 0.02	4.04 ± 0.03
16.70 ± 0.26	7.29 ± 0.07	4.79 ± 0.08	...		
6	21825	131.43290	−43.45194	...	...
...	0.00162 ± 0.00005	0.0088 ± 0.0002	0.053 ± 0.001	0.411 ± 0.006	0.0120 ± 0.0005
0.027 ± 0.001	0.053 ± 0.002	0.082 ± 0.002	0.361 ± 0.006	1.96 ± 0.02	1.98 ± 0.04
...	...	...	...		
7	22262	131.43750	−43.44786	...	...
0.0021 ± 0.0001	0.00712 ± 0.00015	0.01389 ± 0.00026	0.0250 ± 0.0008	0.1386 ± 0.0034	0.00544 ± 0.00017
0.007139 ± 0.000290	0.011046 ± 0.000435	0.013362 ± 0.000505	0.000587 ± 0.000000	...	0.659356 ± 0.000453
...	...	...	...		
8	23011	131.44509	−43.38967	...	...
...	...	...	...	...	0.000487 ± 0.000025
0.00157 ± 0.00007	0.00310 ± 0.00009	0.00297 ± 0.00009	0.0579 ± 0.0015	0.71 ± 0.02	0.86 ± 0.03
2.08 ± 0.02	2.12 ± 0.05	2.09 ± 0.06	...		
9	24056	131.45576	−43.88890	...	0.00081 ± 0.00009
0.0020 ± 0.0001	...	...	...	...	0.0033 ± 0.0001
0.0043 ± 0.0002	...	...	0.056 ± 0.001	0.432 ± 0.014	2.66 ± 0.02
10.16 ± 0.08	4.36 ± 0.04	8.84 ± 0.08	...		
10	26276	131.47872	−43.91127	0.00116 ± 0.00009	0.0028 ± 0.0002
0.0049 ± 0.0002	0.0064 ± 0.0001	0.0066 ± 0.0001	0.0064 ± 0.0003	0.021 ± 0.002	0.0052 ± 0.0005
0.0055 ± 0.0005	0.0048 ± 0.0003	0.0044 ± 0.0002	0.0226 ± 0.0007	...	...
2.84 ± 0.07	1.44 ± 0.04	0.940 ± 0.015	...		
11	37210	131.58937	−43.66819	...	0.00026 ± 0.00009
0.00067 ± 0.00009	0.00068 ± 0.00002	0.00180 ± 0.00004	0.0011 ± 0.0002	0.0183 ± 0.0011	0.00165 ± 0.00004
0.00200 ± 0.00007	0.00210 ± 0.00008	0.00212 ± 0.00006	0.0154 ± 0.0006	...	...
1.63 ± 0.03	2.42 ± 0.03	0.52 ± 0.04	...		
12	38922	131.60656	−43.90894	0.00074 ± 0.000078	0.0030 ± 0.0001
0.0061 ± 0.0002	0.0121 ± 0.0003	0.0210 ± 0.0004	0.0367 ± 0.0008	0.160 ± 0.004	0.0132 ± 0.0003
0.0193 ± 0.0005	0.0262 ± 0.0005	0.0374 ± 0.0008	0.1066 ± 0.0046	...	1.76 ± 0.02
...	...	...	...		
13	39571	131.61333	−43.91638	...	0.00113 ± 0.00010
0.0020 ± 0.0001	...	...	...	...	0.00164 ± 0.00004
0.00158 ± 0.00007	0.00131 ± 0.00004	0.00091 ± 0.00006	...	...	6.95 ± 0.04
12.08 ± 0.07	...	...	...		
14	39589	131.61359	−43.71115	...	...
...	...	...	...	...	0.00147 ± 0.00004
0.00213 ± 0.00005	0.00290 ± 0.00006	0.0042 ± 0.0001	0.121 ± 0.004	3.19 ± 0.01	6.97 ± 0.05
21.65 ± 0.13	9.95 ± 0.07	5.31 ± 0.55	...		
15	41657	131.63487	−43.54801	...	...

Table 5
(Continued)

ID	PSC[b]	R.A.	Decl.	$F_J \pm \Delta F_J$	$F_H \pm \Delta F_H$
$F_K \pm \Delta F_K$	$F_{W1} \pm \Delta F_{W1}$	$F_{W2} \pm \Delta F_{W2}$	$F_{W3} \pm \Delta F_{W3}$	$F_{W4} \pm \Delta F_{W4}$	$F_{3.6} \pm \Delta F_{3.6}$
$F_{4.5} \pm \Delta F_{4.5}$	$F_{5.8} \pm \Delta F_{5.8}$	$F_{8.0} \pm \Delta F_{8.0}$	$F_{24} \pm \Delta F_{24}$	$F_{70} \pm \Delta F_{70}$	$F_{160} \pm \Delta F_{160}$
$F_{250} \pm \Delta F_{250}$	$F_{350} \pm \Delta F_{350}$	$F_{500} \pm \Delta F_{500}$	$F_{1200} \pm \Delta F_{1200}$[c]		
...	...	...	...	...	0.000027 ± 0.000002
0.000030 ± 0.000002	...	...	0.0201 ± 0.0005	...	0.584 ± 0.009
1.48 ± 0.02	2.17 ± 0.03	2.03 ± 0.02	...		
16	42629	131.64522	−43.90839	...	0.0092 ± 0.0007
0.093 ± 0.003	0.966 ± 0.056	4.8 ± 0.6	14.7 ± 0.1	84.7 ± 0.2	0.85 ± 0.03
1.87 ± 0.07	3.67 ± 0.11	3.4 ± 0.6	>4[d]	458.6 ± 2.7	356.4 ± 1.8
458.6 ± 8.0	249.8 ± 1.7	116.3 ± 0.6	8.79		
17	47368	131.69429	−43.33628	...	...
0.00088 ± 0.00010	0.00200 ± 0.00005	0.00424 ± 0.00008	0.0166 ± 0.0004	0.0585 ± 0.0031	0.00373 ± 0.00008
0.0056 ± 0.0001	0.0085 ± 0.0002	0.0125 ± 0.0002	...	...	0.320 ± 0.004
1.357 ± 0.008	1.626 ± 0.015	...	...		
18	47436	131.69495	−43.88731	...	...
...	0.00095 ± 0.00003	0.00333 ± 0.00007	0.0156 ± 0.0003	0.251 ± 0.005	0.00163 ± 0.00006
0.0030 ± 0.0001	0.00370 ± 0.00008	0.00382 ± 0.00007	0.114 ± 0.002	0.780 ± 0.005	1.95 ± 0.01
...	...	...	...		
19	48046	131.70117	−43.88612	...	...
...	...	...	...	...	0.00098 ± 0.00002
0.00255 ± 0.00006	0.00409 ± 0.00009	0.00522 ± 0.00008	0.114 ± 0.007	1.83 ± 0.02	3.63 ± 0.04
...	...	...	...		
20	50748	131.72791	−43.87676	...	...
0.00068 ± 0.00009	0.00199 ± 0.00009	0.0082 ± 0.0002	0.0297 ± 0.0007	0.131 ± 0.004	0.0053 ± 0.0001
0.0114 ± 0.0003	0.0212 ± 0.0004	0.0298 ± 0.0005	0.154 ± 0.003	0.540 ± 0.012	0.754 ± 0.015
2.26 ± 0.04	...	6.40 ± 0.02	...		
21	58569	131.80015	−43.37957	...	...
...	0.00164 ± 0.00006	0.0083 ± 0.0002	0.0121 ± 0.0004	0.089 ± 0.003	0.0026 ± 0.0002
0.0070 ± 0.0005	0.0110 ± 0.0006	0.0133 ± 0.0007	0.089 ± 0.005	2.55 ± 0.03	2.43 ± 0.06
3.92 ± 0.20	3.70 ± 0.06	2.42 ± 0.02	...		
22	59696	131.80945	−43.30581	0.0033 ± 0.0001	0.0074 ± 0.0002
0.0113 ± 0.0004	0.0199 ± 0.0007	0.032 ± 0.001	0.051 ± 0.002	0.147 ± 0.007	0.0194 ± 0.0005
0.0286 ± 0.0008	0.034 ± 0.001	0.0409 ± 0.0008	0.27 ± 0.04	1.21 ± 0.04	2.50 ± 0.03
3.80 ± 0.03	1.94 ± 0.04	1.52 ± 0.02	...		
23	65153	131.85542	−43.81557	...	...
...	...	...	...	...	0.0088 ± 0.0002
0.0183 ± 0.0006	0.0357 ± 0.0006	0.050 ± 0.001	0.49 ± 0.01	1.88 ± 0.02	2.90 ± 0.06
5.79 ± 0.03	3.02 ± 0.04	2.06 ± 0.04	...		
24	65982	131.86223	−43.45189	...	0.00058 ± 0.00008
0.00235 ± 0.00012	0.00080 ± 0.00002	0.00294 ± 0.00005	0.00837 ± 0.00063	0.0456 ± 0.0023	0.00534 ± 0.00015
0.00807 ± 0.00015	0.0118 ± 0.0002	0.01596 ± 0.00022	0.0520 ± 0.0010	0.543 ± 0.004	...
...	...	...	...		
25	68231	131.88064	−43.89669	...	...
...	0.00108 ± 0.00003	0.0068 ± 0.0001	0.0055 ± 0.0004	0.046 ± 0.002	0.00142 ± 0.00005
0.0044 ± 0.0001	0.0069 ± 0.0002	0.0068 ± 0.0002	0.042 ± 0.004	0.767 ± 0.005	2.66 ± 0.07
5.22 ± 0.03	2.78 ± 0.03	...	...		
26	72151	131.91048	−43.82592	...	...
...	0.00021 ± 0.00002	0.00063 ± 0.00002	...	0.024 ± 0.002	0.00038 ± 0.00001
0.00047 ± 0.00002	0.00031 ± 0.00003	...	0.0100 ± 0.0003	...	1.19 ± 0.01
6.06 ± 0.03	5.54 ± 0.02	5.86 ± 0.02	...		
27	72976	131.91688	−43.43769	0.00047 ± 0.00005	0.00216 ± 0.00012
0.00415 ± 0.00015	...	...	...	...	0.00640 ± 0.00019
0.00621 ± 0.00012	0.00643 ± 0.00014	0.00568 ± 0.00010	...	...	4.409 ± 0.018
7.35 ± 0.65	8.95 ± 0.07	...	...		
28	83949	131.99760	−43.65348	...	...
0.0011 ± 0.0001	0.00284 ± 0.00007	0.0056 ± 0.0001	...	0.007 ± 0.002	0.0023 ± 0.0001
0.0032 ± 0.0002	0.0041 ± 0.0002	0.0043 ± 0.0001	0.0135 ± 0.0005	...	1.44 ± 0.02
4.55 ± 0.02	3.07 ± 0.03	...	...		
29	86208	132.01412	−43.85429	0.00275 ± 0.00012	0.00684 ± 0.00027
0.00938 ± 0.00031	0.01279 ± 0.00027	0.01784 ± 0.00033	0.0569 ± 0.0010	0.1436 ± 0.0038	0.01606 ± 0.00037

Table 5
(Continued)

ID	PSC[b]	R.A.	Decl.	$F_J \pm \Delta F_J$	$F_H \pm \Delta F_H$
$F_K \pm \Delta F_K$	$F_{W1} \pm \Delta F_{W1}$	$F_{W2} \pm \Delta F_{W2}$	$F_{W3} \pm \Delta F_{W3}$	$F_{W4} \pm \Delta F_{W4}$	$F_{3.6} \pm \Delta F_{3.6}$
$F_{4.5} \pm \Delta F_{4.5}$	$F_{5.8} \pm \Delta F_{5.8}$	$F_{8.0} \pm \Delta F_{8.0}$	$F_{24} \pm \Delta F_{24}$	$F_{70} \pm \Delta F_{70}$	$F_{160} \pm \Delta F_{160}$
$F_{250} \pm \Delta F_{250}$	$F_{350} \pm \Delta F_{350}$	$F_{500} \pm \Delta F_{500}$	$F_{1200} \pm \Delta F_{1200}$[c]		
0.01977 ± 0.00066	0.02691 ± 0.00055	0.04102 ± 0.00059	0.1091 ± 0.0016	...	3.11 ± 0.02
10.07 ± 0.06	5.43 ± 0.03	2.73 ± 0.02	...		
30	113290	132.22921	−43.71078	...	...
...	...	...	...	...	0.000164 ± 0.000004
0.000104 ± 0.000004	...	...	0.0191 ± 0.0033	...	0.461 ± 0.006
1.017 ± 0.02	1.44 ± 0.02	...	...		
31	123062	132.32596	−43.93661	...	...
0.00069 ± 0.00009	0.00121 ± 0.00005	0.00227 ± 0.00005	0.0061 ± 0.0002	0.021 ± 0.001	0.00172 ± 0.00005
0.00246 ± 0.00005	0.00316 ± 0.00006	0.00331 ± 0.00005	0.0081 ± 0.0004	...	0.777 ± 0.006
2.19 ± 0.20	...	0.970 ± 0.007	...		
32	124358	132.33936	−44.03091	...	...
...	...	...	...	...	0.00110 ± 0.00002
0.00208 ± 0.00007	0.00319 ± 0.00007	0.00455 ± 0.00008	...	2.31 ± 0.03	3.52 ± 0.04
5.84 ± 0.04	4.32 ± 0.05	3.33 ± 0.08	...		
33	127425	132.37080	−43.99599	...	...
...	...	...	...	...	0.00050 ± 0.00001
0.00054 ± 0.00002	0.00055 ± 0.00002	0.00052 ± 0.00001	...	...	0.899 ± 0.005
2.09 ± 0.06	2.02 ± 0.02	1.63 ± 0.02	...		

Notes.
[a] Coordinates are given in degrees; fluxes (F) and their uncertainties (ΔF) are given in Jy.
[b] ID in the VMR-D PSC catalog (Paper I).
[c] The uncertainty of the 1.2 mm flux is 20% (Massi et al. 2007).

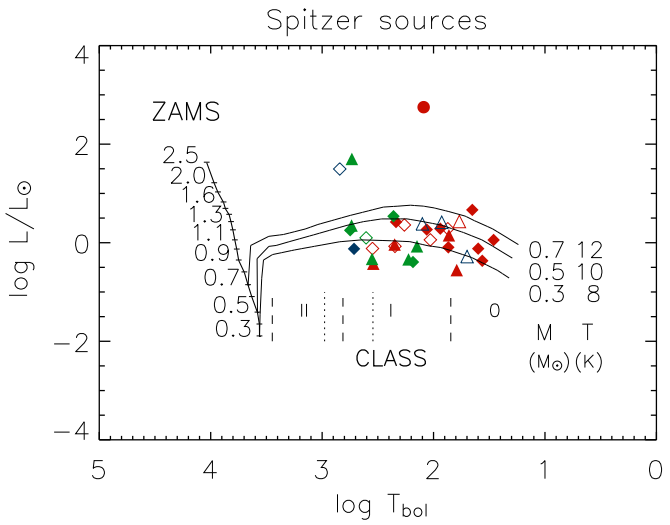

Figure 8. Bolometric luminosity–temperature diagram obtained for the *Spizer* ON-cloud YSOs. By using the classification criteria based on the MIR spectral slope, red symbols correspond to Class I, green is used for FS, and blue is used for Class II sources. Different symbols denote different FIR spectral coverage: the filled circle is an object with *Herschel*-SPIRE fluxes, as well as 24 μm and 1.2 mm fluxes. Diamonds denote sources with 24 μm flux but undetected at 1.2 mm, with (filled) and without (open) *Herschel*-SPIRE fluxes, respectively. Finally, triangles are objects without 1.2 mm flux and at least two fluxes in the 70–500 μm range, but with (filled) and without (open) 24 μm flux, respectively. Evolutionary tracks are taken from Myers et al. (1998) and are labeled with the final stellar mass and the initial temperature of the outer envelope. In the bottom panel, with dashed lines, the correspondence between T_{bol} and spectral class as defined by Chen et al. (1995) is reported for comparison. The boundaries of the FS sources as suggested by Evans et al. (2009) are also reported with dotted lines.

opportunity to complete our information on the early objects. From this perspective the bolometric temperature and luminosity for the 30 protostellar and 92 starless *Herschel* ON-cloud sources have been computed by using the merged FIR catalog described in Section 2.2. However, this catalog also includes complementary fluxes in the MIR spectral range so that we always use all the available fluxes, which for the ON-cloud protostars are reported in Table 6, to obtain the source luminosities. The resulting luminosity distribution is shown in the right panel of Figure 7, where a trend is apparent for the protostars to be, on average, more luminous than the starless cores. As expected, an opposite trend can be seen in the size distribution shown in the left panel, where the protostellar sources appear as more compact objects with respect to the starless ones.

By computing the bolometric temperatures from Equation (3), we also obtain the corresponding luminosity–temperature diagram that is shown in Figure 9. It can be directly compared with Figure 8 because both refer to the same region of the VMR-D, namely, the intersection between the *Herschel* coverage, the *Spitzer*-PSC catalog, and the ON-cloud region that is shown in Figure 1. In the same figure the positions of both the *Spitzer*- and *Herschel*-selected sources are also shown.

Among these *Herschel*-selected protostars we also find cases with $T_{bol} < 70$ K that can be classified as Class 0 objects, even though in this case they are relatively more abundant (17 out of 30 protostars) than in the *Spitzer*-selected sample. This is clearly as expected because the earlier phases, corresponding to colder objects, are more easily detected at the longer wavelengths of the *Herschel* observations.

It is, however, noteworthy that 10 out of the 30 *Herschel* protostars are also detected by *Spitzer*, so that the total number of protostars in this region amounts to 53 sources. We then find

Table 6
Photometry of the *Herschel*-selected Protostars[a]

ID	R.A.	Decl.	$F_{W1} \pm \Delta F_{W1}$	$F_{W2} \pm \Delta F_{W2}$	$F_{W3} \pm \Delta F_{W3}$
$F_{W4} \pm \Delta F_{W4}$	$F_{3.6} \pm \Delta F_{3.6}$	$F_{4.5} \pm \Delta F_{4.5}$	$F_{5.8} \pm \Delta F_{5.8}$	$F_{8.0} \pm \Delta F_{8.0}$	$F_{24} \pm \Delta F_{24}$
$F_{BLUE} \pm \Delta F_{BLUE}$	$F_{RED} \pm \Delta F_{RED}$	$F_{PSW} \pm \Delta F_{PSW}$	$F_{PMW} \pm \Delta F_{PMW}$	$F_{PLW} \pm \Delta F_{PLW}$	$F_{1200} \pm \Delta F_{1200}$[b]
1	131.18478	−43.70255	0.00221 ± 0.00005	0.00141 ± 0.00003	0.0025 ± 0.0004
0.046 ± 0.001	0.00053 ± 0.00004	0.00060 ± 0.00002	0.00067 ± 0.00003	0.00095 ± 0.00003	0.045 ± 0.001
0.35 ± 0.01	0.69 ± 0.01	1.51 ± 0.03	0.72 ± 0.09	0.49 ± 0.01	···
2	131.28860	−43.63342	0.00016 ± 0.00001	0.00025 ± 0.00005	0.0027 ± 0.0003
0.0165 ± 0.0013	0.000044 ± 0.000003	0.00014 ± 0.00001	···	0.000091 ± 0.000020	0.0171 ± 0.0007
0.63 ± 0.02	1.09 ± 0.02	2.70 ± 0.03	3.08 ± 0.04	1.63 ± 0.03	···
3	131.39476	−43.85289	···	···	···
···	0.00175 ± 0.00008	0.00166 ± 0.00005	0.0041 ± 0.0002	0.0091 ± 0.0007	···
19.4 ± 0.5	17.48 ± 0.44	40.6 ± 0.2	27.0 ± 0.1	···	3.17
4	131.40118	−43.86400	···	···	···
···	0.0015 ± 0.0001	0.0016 ± 0.0001	0.0083 ± 0.0009	···	···
61.65 ± 0.17	76.48 ± 0.18	87.56 ± 0.60	93.30 ± 0.50	···	3.70
5	131.41060	−43.91772	0.0233 ± 0.0005	0.0406 ± 0.0007	0.062 ± 0.001
0.259 ± 0.005	0.0263 ± 0.0007	0.033 ± 0.001	0.0420 ± 0.0008	0.050 ± 0.001	0.194 ± 0.008
0.483 ± 0.012	4.04 ± 0.03	16.70 ± 0.26	7.29 ± 0.07	4.79 ± 0.08	···
6	131.42451	−43.86047	···	···	···
···	···	···	···	···	···
8.70 ± 0.06	54.36 ± 0.35	120.98 ± 0.11	75.20 ± 0.19	···	···
7	131.42975	−43.45671	0.00322 ± 0.00007	0.0156 ± 0.0003	0.0076 ± 0.00062
0.0937 ± 0.0027	0.00240 ± 0.00009	0.0052 ± 0.0002	0.0076 ± 0.0003	0.0080 ± 0.0003	···
0.623 ± 0.009	2.70 ± 0.05	6.82 ± 0.03	4.59 ± 0.05	3.87 ± 0.04	···
8	131.44052	−43.43735	···	···	···
···	0.0026 ± 0.0002	0.0037 ± 0.0002	0.0044 ± 0.0002	0.0033 ± 0.0001	···
0.399 ± 0.006	1.58 ± 0.01	5.62 ± 0.06	2.85 ± 0.04	1.66 ± 0.09	···
9	131.44492	−43.38979	···	···	···
···	0.00049 ± 0.00002	0.00157 ± 0.00007	0.0031 ± 0.0001	0.0030 ± 0.0001	0.0579 ± 0.0015
0.707 ± 0.009	0.860 ± 0.008	2.08 ± 0.02	2.12 ± 0.04	2.09 ± 0.16	···
10	131.44581	−43.41722	···	···	···
···	···	···	···	0.000000 ± 0.000000	0.000000 ± 0.000000
0.847 ± 0.009	1.47 ± 0.01	4.92 ± 0.02	2.70 ± 0.03	2.79 ± 0.09	···
11	131.52779	−43.66405	···	···	···
···	0.00037 ± 0.00002	0.00048 ± 0.00002	0.0011 ± 0.0001	0.0020 ± 0.0001	···
2.02 ± 0.02	6.94 ± 0.03	16.22 ± 0.06	···	9.23 ± 0.09	···
12	131.58482	−43.47723	0.00029 ± 0.00002	0.00040 ± 0.00002	···
0.005 ± 0.002	0.00046 ± 0.00002	0.00048 ± 0.00002	0.00055 ± 0.00002	0.00286 ± 0.00005	0.0071 ± 0.0002
0.56 ± 0.01	0.61 ± 0.04	1.00 ± 0.02	0.74 ± 0.01	0.64 ± 0.01	···
13	131.61105	−43.70360	0.0056 ± 0.0001	0.0041 ± 0.00009	0.073 ± 0.001
0.137 ± 0.004	0.0035 ± 0.0001	0.00251 ± 0.00007	0.0079 ± 0.0007	0.016 ± 0.002	0.13 ± 0.02
5.14 ± 0.04	15.30 ± 0.07	15.24 ± 0.06	···	···	2.78
14	131.61224	−43.93114	···	···	···
···	0.00029 ± 0.00001	0.00087 ± 0.00004	0.00099 ± 0.00005	0.0004 ± 0.0001	···
1.32 ± 0.02	5.86 ± 0.09	7.938 ± 0.042	5.053 ± 0.024	7.27 ± 0.040	···
15	131.63194	−43.93623	0.0120 ± 0.0003	0.0119 ± 0.0002	0.275 ± 0.003
3.02 ± 0.07	···	···	···	···	···
38.88 ± 0.23	27.91 ± 0.25	8.41 ± 0.15	19.20 ± 0.09	···	···
16	131.63538	−43.54644	···	0.00044 ± 0.00001	···
0.023 ± 0.001	0.00019 ± 0.00001	0.00051 ± 0.00003	0.00066 ± 0.00003	0.00085 ± 0.00004	0.0201 ± 0.0005
0.26 ± 0.01	0.58 ± 0.01	1.48 ± 0.02	2.17 ± 0.03	2.03 ± 0.02	···
17	131.64540	−43.91031	···	···	···
···	0.85 ± 0.03	1.87 ± 0.07	3.666 ± 0.115	3.4 ± 0.6	>4.0[c]
458.6 ± 2.7	356.4 ± 1.8	458.6 ± 8.0	249.8 ± 1.7	116.3 ± 0.6	···
18	131.80005	−43.37969	0.00164 ± 0.00006	0.0083 ± 0.0002	0.0121 ± 0.0004
0.089 ± 0.003	0.0026 ± 0.0002	0.0070 ± 0.0005	0.0111 ± 0.0006	0.0133 ± 0.0007	0.089 ± 0.004
2.55 ± 0.03	2.43 ± 0.06	···	3.70 ± 0.06	2.42 ± 0.02	···
19	131.80984	−43.30710	0.056 ± 0.001	0.091 ± 0.002	0.159 ± 0.002
0.308 ± 0.008	0.054 ± 0.002	0.074 ± 0.002	0.105 ± 0.003	0.125 ± 0.002	0.27 ± 0.04
1.21 ± 0.04	2.50 ± 0.03	3.80 ± 0.03	1.94 ± 0.04	1.52 ± 0.02	···

Table 6
(Continued)

ID	R.A.	Decl.	$F_{W1} \pm \Delta F_{W1}$	$F_{W2} \pm \Delta F_{W2}$	$F_{W3} \pm \Delta F_{W3}$
$F_{W4} \pm \Delta F_{W4}$	$F_{3.6} \pm \Delta F_{3.6}$	$F_{4.5} \pm \Delta F_{4.5}$	$F_{5.8} \pm \Delta F_{5.8}$	$F_{8.0} \pm \Delta F_{8.0}$	$F_{24} \pm \Delta F_{24}$
$F_{BLUE} \pm \Delta F_{BLUE}$	$F_{RED} \pm \Delta F_{RED}$	$F_{PSW} \pm \Delta F_{PSW}$	$F_{PMW} \pm \Delta F_{PMW}$	$F_{PLW} \pm \Delta F_{PLW}$	$F_{1200} \pm \Delta F_{1200}$[b]
20	131.85530	−43.81571	0.0185 ± 0.0004	0.0432 ± 0.0008	0.109 ± 0.002
0.46 ± 0.01	0.0088 ± 0.0002	0.0183 ± 0.0006	0.0357 ± 0.0006	0.050 ± 0.001	0.49 ± 0.01
1.88 ± 0.02	2.90 ± 0.06	5.79 ± 0.03	3.02 ± 0.04	2.06 ± 0.04	...
21	131.88019	−43.89773	0.00108 ± 0.00003	0.0068 ± 0.0001	0.0055 ± 0.0003
0.046 ± 0.002	0.00031 ± 0.00001	0.00085 ± 0.00003	0.00143 ± 0.00004	0.00168 ± 0.00003	0.042 ± 0.004
0.77 ± 0.01	2.66 ± 0.07	5.22 ± 0.03	2.78 ± 0.03	6.82 ± 0.02	...
22	131.92834	−43.73021	0.0280 ± 0.0006	0.090 ± 0.001	0.330 ± 0.003
2.24 ± 0.02	0.042 ± 0.002	0.079 ± 0.002	0.124 ± 0.003	0.180 ± 0.004	1.16 ± 0.08
14.35 ± 0.05	10.99 ± 0.06	13.90 ± 0.03	5.23 ± 0.03	5.75 ± 0.06	0.103
23	131.96498	−43.42231	0.0040 ± 0.0002	0.0090 ± 0.0002	0.094 ± 0.001
0.205 ± 0.006	0.0029 ± 0.0002	0.0056 ± 0.0002	0.0098 ± 0.0002	0.0125 ± 0.0003	0.10 ± 0.01
1.26 ± 0.02	4.14 ± 0.03	6.06 ± 0.08	2.45 ± 0.03	0.968 ± 0.011	...
24	132.06612	−43.78766	...	...	...
...	0.000013 ± 0.000003	0.00030 ± 0.00001	0.00004 ± 0.00003	...	0.0268 ± 0.0007
15.08 ± 0.11	13.60 ± 0.08	11.90 ± 0.12	5.75 ± 0.04	3.66 ± 0.06	0.061
25	132.10312	−43.53003	...	...	...
...	...	...	...	...	...
0.190 ± 0.004	1.69 ± 0.01	4.40 ± 0.02	5.40 ± 0.04	...	...
26	132.14529	−43.91617	0.00218 ± 0.00005	0.0051 ± 0.0001	0.0078 ± 0.0002
0.033 ± 0.002	0.00392 ± 0.00009	0.0059 ± 0.0001	0.0082 ± 0.0002	0.0099 ± 0.0001	0.021 ± 0.001
0.503 ± 0.004	1.27 ± 0.03	3.71 ± 0.03	3.36 ± 0.05	2.73 ± 0.02	...
27	132.17854	−43.61838	0.00063 ± 0.00005	0.00059 ± 0.00003	...
...	...	0.00031 ± 0.00002	0.00029 ± 0.00002	...	0.0031 ± 0.0009
0.413 ± 0.003	1.54 ± 0.02	6.00 ± 0.02	6.50 ± 0.09	...	0.133
28	132.32057	−43.93255	...	...	...
...	...	0.00031 ± 0.00003	...	0.00053 ± 0.00003	0.0134 ± 0.0005
1.52 ± 0.02	2.15 ± 0.03	2.81 ± 0.08	1.66 ± 0.01	0.970 ± 0.007	...
29	132.33763	−44.03125	...	...	...
...	...	...	...	...	0.044 ± 0.004
2.31 ± 0.03	3.52 ± 0.04	5.84 ± 0.04	4.32 ± 0.05	3.33 ± 0.08	...
30	132.36937	−44.07478	...	0.00099 ± 0.00003	...
...	0.00033 ± 0.00005	0.0010 ± 0.0001	0.0016 ± 0.0002	0.00041 ± 0.00007	0.0049 ± 0.0005
3.96 ± 0.03	5.33 ± 0.03	6.79 ± 0.02	3.77 ± 0.04	3.06 ± 0.03	0.136

Notes.
[a] Coordinates are given in degrees; fluxes (F) and their uncertainties (ΔF) are given in Jy.
[b] The uncertainty of the 1.2 mm flux is 20% (Massi et al. 2007).

that the *Herschel* observations are necessary to reveal 20 new protostars, corresponding to approximately one-third of the total population in the surveyed part of the VMR-D cloud.

For the protostars in common, in Table 7 we report the classification determined by using the two schemes parameterized by the MIR spectral slope (Lada 1987) and by the bolometric temperature (Chen et al. 1995; Evans et al. 2009), respectively.

Considering now that the angular extension of our ON-cloud investigated region is ∼0.48 deg^2 and that we adopted a nominal distance of 700 pc for the VMR-D, we find a protostellar surface density of ∼0.7 pc^{-2}. A comparison with the SF scaling law derived by Lombardi et al. (2013) for the Orion molecular cloud suggests that the VMR-D protostellar density would be compatible with a visual extinction $A_V \sim 5.5$, a value we find inside our ON-cloud region delimited by $A_V \sim 3.5$.

Table 7
Protostars Detected by Both *Spitzer* and *Herschel*

NAME	R.A.	Decl.	Classification		$\Delta\Theta$[a]
Spitzer-PSC	(deg)	(deg)	MIR[b]	FIR[c]	(″)
8036	131.28840	−43.63255	I	0	3.1
23011	131.44509	−43.38967	I	I	0.7
41657	131.63487	−43.54801	I	0	6.0
42629	131.64522	−43.90839	I	I	6.9
58569	131.80015	−43.37957	I	I	0.6
65153	131.85542	−43.81557	I	I	0.6
68231	131.88064	−43.89669	I	0	3.9
124358	132.33936	−44.03091	I	0	6.4
19667	131.41093	−43.91746	FS	I	1.4
59696	131.80945	−43.30581	FS	FS	4.7

Notes.
[a] Distance between the positions reported in the MIR and FIR catalogs.
[b] Based on the slope in the 2–24 μm spectral range.
[c] Based on the value of the bolometric temperature (see text).

6. DISCUSSION

A preliminary analysis of the young stellar population in the VMR-D cloud was presented in Paper I, but it was limited

Table 8
Comparison of the *Spitzer* YSOs in VMR-D with Other SFRs

Region	Area (deg^2)	Dist (pc)	YSO	YSO (deg^{-2})	YSO (pc^{-2})	Class I	Flat	Class II	Class III
This work	0.54	700	499	925	6.1	82 (17%)	52 (10%)	129 (26%)	236 (47%)
Paper I	"	"	297	522	3.5	39 (13.2%)	51 (17.3%)	142 (47.6%)	65 (21.9%)
Cha II	1.04	178	26	25	2.6	2 (8%)	1 (4%)	19 (73%)	4 (15%)
Lupus	3.10	150	94	30	3.3	5 (5%)	10 (11%)	52 (55%)	27 (29%)
Perseus	3.86	250	385	100	5.2	87 (23%)	42 (11%)	225 (58%)	31 (8%)
Serpens	0.85	260	227	267	13	36 (16%)	23 (10%)	140 (62%)	28 (12%)
Ophiucus	6.60	125	292	44	9.3	35 (12%)	47 (16%)	176 (60%)	34 (12%)

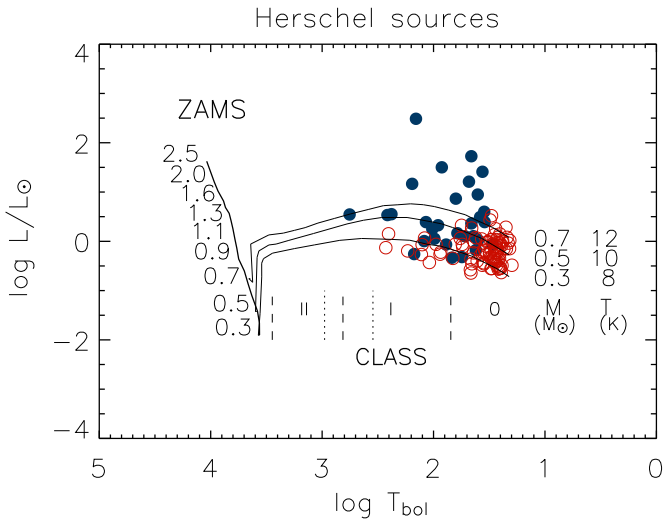

Figure 9. Bolometric luminosity–temperature diagram obtained for sources detected by *Herschel*. Filled blue circles are used for protostars, while open red circles represent starless sources. The statistics of the protostars are summarized in Table 4, their fluxes are summarized in Table 6, and their positions in the VMR-D cloud are shown in Figure 1. Ten protostars, listed in Table 7, are in common with Figure 8.

to the sources detected in all four *Spitzer*-IRAC bands. Now, considering the full sample of the *Spitzer*-PSC sources and adopting a more demanding selection procedure, we obtain a more complete and reliable set of candidate YSOs to derive more accurate global properties of the SF in this cloud. Table 8 summarizes our results and, for the sake of comparison, also reports the results obtained by Evans et al. (2009) for the SF regions of the c2d *Spitzer* legacy program. The comparison with Paper I shows that despite the addition of sources detected in only three or even two IRAC bands, the number of FS and Class II candidate YSOs is similar as a result of adopting more stringent criteria to reject reddened photospheres in the selection pipeline (see Table 2 and Figure 2). On the other hand, we select more Class I objects because a significant number of additional sources, detected in three or two IRAC bands, cannot be fitted by reddened photospheres and pass all the subsequent color–color and color–magnitude selection criteria discussed in Section 3. These are mainly sources detected at 3.6 and 4.5 μm, namely, in the two more sensitive IRAC bands that are approximately 10 times more sensitive than the 5.8 and 8.0 μm bands. The flux distribution of these additional sources peaks around 0.1 mJy, showing that at these wavelengths they are faint objects near the completeness limit of the *Spitzer*-PSC catalog (see Table 1). Note, however, that for the sake of a robust detection, these sources have been included in our analysis only if they also show an MIPS 24 μm counterpart.

Similarly, the number of Class III objects is noticeably larger than that quoted in Paper I. In this case the additional sources are mainly detected only in the first three IRAC bands. Despite that a large fraction of these three-band sources are actually discarded as reddened photospheres, a still consistent number survive our selection steps, showing fluxes brighter than 0.1 mJy with a distribution peaking at 0.4, 0.3, and 0.25 mJy in the first three IRAC bands, respectively. In this respect we must consider that the VMR-D line of sight crosses the Galactic plane and thus is particularly contaminated by giant stars that because of their thin dust envelopes, can closely mimic a Class III SED, making it difficult to distinguish them from genuine YSOs. In this respect we recall that the 8 μm PAH emission, which can be produced in carbon-rich red giant envelopes as well as in blobs of nebulosity, could also bias the selection of Class III sources, in particular for the faint objects. Despite our efforts to mitigate this problem by adopting appropriate color constraints in Section 3 and by subtracting the surface density of the YSOs seen outside the cloud (see Table 3), we consider that the number of Class III sources quoted in Tables 3 and 8 is the most uncertain.

6.1. Comparison with Other SFRs

To compare the relative abundance of the different classes in VMR-D with those characterizing other SFRs, we show in Figure 10 the number ratios for Class I, FS, and Class II sources obtained in the different studies based on *Spitzer* observations, along with their uncertainties evaluated by assuming Poisson statistics. In this diagram the Class I/FS ratio for the VMR-D is well in the range of the other SFRs, while the (ClassI+FS)/Class II ratio appears clearly displaced toward the largest values. A possible systematic shift in this diagram could be produced by the interstellar reddening, which tends to steepen the spectral slope and then to produce a bias in the classification favoring the earlier classes. However, reasonable values of the interstellar extinction toward VMR-D do not significantly influence the position in this diagram, as is shown by the arrow in Figure 10, which represents the effect of an interstellar extinction $A_V = 5$ mag. Given the values estimated for the interstellar extinction toward VMR-D ($A_V \sim 2$ mag, Cambresy 1999; Joshi 2005), we find that the offset position of the VMR-D in this diagram cannot be explained by this effect and thus more probably reflects an intrinsic difference in the relative populations. That this can be the case is also shown by the work of Hsieh & Lai (2013), who noted that the relative number of the YSOs in Perseus significantly changes if one considers the whole region or, separately, the two subregions extending eastward and westward of R.A. = 54.°3. To illustrate this point, in Figure 10 we also report these two subregions as EPer and

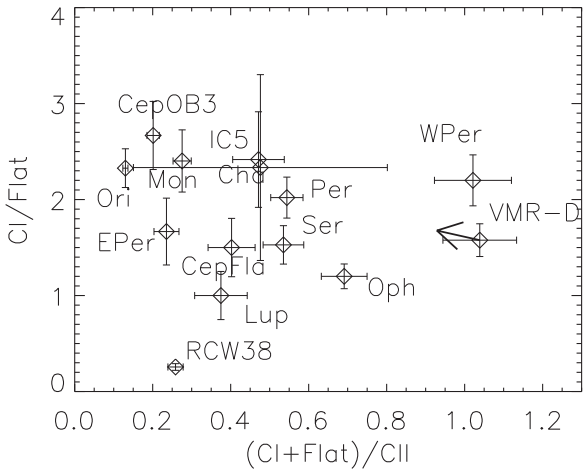

Figure 10. Class I/FS vs. (Class I+FS)/Class II number ratio for *Spitzer* sources detected in different clouds. VMR-D and WPer show a larger content of Class I and FS sources with respect to the other SFRs. An arrow shows the displacement produced in the VMR-D position by correcting for an extinction of $A_V = 5$ mag. Data for other clouds are taken from Hsieh & Lai (2013) for the c2d SFRs (Cha, Lup, Per, Ser, and Oph, as well as EPer and WPer, representing the eastern and western regions in Perseus, respectively). For RCW 38, Cep, and IC 5146 we used the data in Winston et al. (2011); Kirk et al. (2009); Harvey et al. (2008), while for Ori, Mon, and CepOB3 we used those given by Kryukova et al. (2012). Note, however, that Kryukova et al. (2012) use more restrictive criteria in selecting FS sources, and this is probably reflected in the upper left position of Ori, Mon, and CepOB3 in this diagram.

Table 9
Comparison of SF Rate, SF Efficiency, and Depletion Time

Region	SFR/Area ($M_\odot$ Myr^{-1} pc^{-2})	SF Efficiency ($M_{YSO}/(M_{cl}+M_{YSO})$)	Depletion (Myr)
This work	2.3	0.014	96
Paper I[a]	1.3	0.01–0.02	90–140
Cha II	0.65	0.030	66
Lupus	0.83	0.054	35
Perseus	1.3	0.038	50
Serpens	3.2	0.053	35
Ophiucus	2.3	0.063	30

Note. [a] Because the assumed mean mass was 1 $M_\odot$ in Paper I, here the values are recalculated for 0.5 $M_\odot$ (see text).

WPer, in this way showing how they diverge from the position occupied by Perseus considered as a whole.

Intuitively, we can guess that, in terms of a single SF burst, early objects are initially favored so that both Class I/FS and (Class I+FS)/Class II number ratios should be relatively high. The absolute value and the time dependence expected for these ratios are clearly related to the specific modeling of the physical processes involved. Here we can only say that if the position in this diagram has an evolutionary meaning, the VMR-D cloud appears much more similar to WPer and Ophiucus than to the other SFRs. However, if the SF occurs in multiple episodes or proceeds as a continuous process, Figure 10 cannot be easily interpreted and theoretical modeling is needed to disentangle the different effects, a matter that is, however, beyond the scope of the present work.

This simplified analysis suffers, however, at least two limits that should be considered in future work: the possibility that Class II reddened disks can appear as FS sources (Dunham et al. 2014), and the presence, among the Class I objects, of cases that could well be Class 0 on the basis of their bolometric

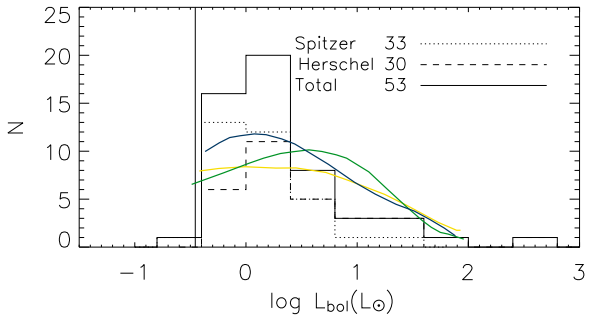

Figure 11. PLF: *Spitzer* (dotted line) and *Herschel* (dashed line) protostars located in the *Spitzer*/*Herschel* overlap region of VMR-D (see Figure 1) and projected ON-cloud. The total luminosity function is shown with a solid line accounting for 10 objects that are common to the two samples. The vertical line represents the completeness limit based on the fluxes quoted in Table 1. Models from Offner & McKee (2011), including competitive accretion (yellow), turbulent core (green), and two-component turbulent core models (blue), are also shown for comparison.

temperature. The first possibility tends to move the individual clouds toward the upper left part of Figure 10, as could be the case for Ori, Mon, and CepOB3, whose FS sources have been selected by Kryukova et al. (2012) with criteria that are more restrictive than those used for the other SFRs. The second point, on the possible presence of some Class 0 among the Class I Objects, should not change the significance of the diagram as long as we simply reconsider that Class 0+I constitutes a single counting bin. In this sense, however, the larger relative content of protostars in VMR-D, WPer, and Oph is noteworthy, suggesting for these regions a more recent SF event.

Once the YSOs are identified, further relevant quantities can be derived that characterize the SF in our cloud. These are reported in Table 9 and are obtained for a distance of 700 pc and under some simplifying assumptions, such as a mean mass of 0.5 $M_\odot$, a binary fraction of 0.5, and an age of 2 Myr (Evans et al. 2009), the latter being an estimate of the time taken to pass through the Class II SED phase. It is interesting that, as for the position of the VMR-D in Figure 10, we also find a greater similarity of the SF rate value to that of the Ophiuchus cloud than to those of the other SFRs.

6.2. Protostellar Luminosity Function

The PLF, determined by using all the protostars we find ON-cloud for which an accurate bolometric luminosity has been obtained in Section 5, is shown in Figure 11. The completeness luminosity $L_{com} \simeq 0.35\,L_\odot$, shown as a vertical line, is evaluated on the basis of the completeness fluxes given in Table 1. In this figure we report only sources located ON-cloud in the overlap region observed by both *Spitzer* and *Herschel*, so that a comparison is possible between the abilities of the two approaches to detect protostars. In particular, we select 33 *Spitzer* and 30 *Herschel* protostellar sources, so that, considering that 10 sources are present in both samples, we conclude that in this region the *Herschel* observations contribute 20 additional protostars to those detected by *Spitzer*, leading to a total of 53 protostars. Taken all together, these produce a more complete and representative PLF, which is shown in Figure 11 with a solid line. In the same figure three curves are also superimposed representing the PLF expected, after 1 Myr evolution, by models considering competitive accretion, turbulent core, and two-component turbulent core, computed by Offner & McKee (2011) with an upper limit for the final stellar mass of 3 $M_\odot$.

Table 10
PLF Statistics in $\log(L/L_\odot)$

Region	N	Mean[a]	Median[a]	σ[a]	Completeness($M_\odot$)	Reference
VMR-D	53	0.31	0.25	0.58	0.35	This work
6 low-mass	122	−0.18(−0.09)	−0.20(−0.13)	0.72(0.78)	0.05–0.01	Kryukova et al. (2012)
3 high-mass	425	0.15(0.28)	0.04(0.18)	0.76(0.77)	0.05–0.03	Kryukova et al. (2012)
18 low-mass	230	−0.03(0.07)	−0.03(0.11)	0.75(0.73)	0.2	Dunham et al. (2013)

Note. [a] Numbers in parentheses are obtained after dereddening.

A comparison with the PLF already known for other clouds suggests that the high-luminosity tail extending beyond 100 $L_\odot$ makes the PLF in VMR-D more similar to those found in the high-mass SFRs (Kryukova et al. 2012). The most luminous source, namely, 42629 in the *Spitzer*-PSC numbering, is a Class I in both classification schemes, based on the MIR spectral slope and the bolometric temperature, and is located in the center of a bright IR cluster (IRS17, Liseau et al. 1992; Massi et al. 2000). A more quantitative comparison with the luminosity distribution obtained in other SFRs is presented in Table 10, which summarizes simple statistics corresponding to high- and low-mass cases. The tabulated values suggest that the PLF in the VMR-D is more similar to that exhibited by the high-mass SFRs, especially after correction of the reddening effect. Note, however, that our luminosities have not been corrected for this effect because they are essentially associated with Class 0 and I objects whose luminosity is dominated by the FIR contribution and is only marginally affected by the extinction.

A much more important difference is due to the completeness luminosity, which in our case is approximately 10 times that quoted by Kryukova et al. (2012). These authors in fact, adopting a remarkable relationship that they find between the bolometric and the MIR luminosity of the YSOs with $\alpha > 0$, derive the bolometric luminosity for a large number of objects with a well-sampled SED in the MIR, in this way exploiting the high sensitivity of *Spitzer*-MIPS 24 μm observations at the risk of an uncertain extrapolation. With this method they sensibly enlarge the number of sources useful to obtain a better coverage of the low-luminosity tail of the distribution. In our case we adopt a more conservative approach and compute the bolometric luminosity of *Spitzer*-selected sources only when at least two good-quality FIR fluxes are actually observed in the 70–500 μm range, with the result of a larger completeness luminosity that is most probably the cause of the differences seen in Table 10.

6.3. Envelope Masses

Because the PLF depends on both mass and time, its relationship to the initial mass function of the stars produced by the protostars is not straightforward. Ideally, one should know both the luminosity and the age of an object to infer its mass on the basis of some theoretical model. In principle, because the contributions to the observed luminosity come from a central object, as well as from a surrounding disk and possibly an envelope, a detailed modeling of the global SED is to be used to disentangle the masses of the different components.

Nevertheless, in the early phases when the protostars appear as a Class 0/I, it is customary to simplify the problem of deriving the envelope mass by assuming that the FIR emission is optically thin and is thus useful to trace the total envelope mass. In our case we could consider the subsample of the ON-cloud protostars with an observed 500 μm flux, assuming that this is produced in an optically thin regime and adopting for the dust temperature the value obtained by fitting the *Herschel* fluxes at $\lambda \geqslant 160$ μm (see Section 3) with the model in Equation (1). However, given that most of our sources are resolved at *Herschel* wavelengths, we can also obtain the masses following the derivation in Pezzuto et al. (2012) that involves the angular extension Ω of the emitting body:

$$M = \frac{D^2 \Omega}{k_{\rm ref}} \left(\frac{\lambda_0}{\lambda_{\rm ref}} \right)^2. \quad (5)$$

This expression allows us to derive the envelope mass for the 30 Herschel protostars (including the 7 cases without a 500 μm flux; see Table 6) because it does not depend explicitly on the observed flux at a given wavelength. This dependence is hidden in the fitting of the observed FIR fluxes with Equation (1), which also gives, as a by-product, the λ_0 value, namely, the wavelength at which $\tau = 1$. Similarly, we also extend this same approach to the starless cores detected in at least three *Herschel* wavelengths at $\lambda \geqslant 160$ μm.

The envelope masses have then been obtained adopting an emission coefficient $k_{\rm ref} = 0.1$ cm^2 g^{-1} of gas mass at $\lambda_{\rm ref} = 250$ μm (Hildebrand 1983; Suutarinen et al. 2013) and a scaling law $k = k_{\rm ref}(\lambda_{\rm ref}/\lambda)^2$. In Figure 12 we present the resulting distribution of the envelope masses (upper panel) computed for both protostellar and starless sources. Because in the latter case the derived values represent the true total mass, it is interesting to compare the derived masses with the Bonnor–Ebert critical mass, approximately given by $M_{\rm BE} \approx 2.4 R_{\rm BE} a^2/G$, with a being the sound speed at the source temperature. Such a comparison offers a simple way to separate prestellar from quiescent cores by simply assuming that masses $M \gtrsim 0.5\ M_{\rm BE}$ are bound and then should be considered as prestellar because they more probably evolve toward a protostar.

Assuming for $R_{\rm BE}$ the observed deconvolved radius at 250 μm, we find that $M > 0.5\ M_{\rm BE}$ for 67 out of 92 ON-cloud sources that we then consider as bound and potentially prestellar. In Figure 12 the distribution of all the starless sources is shown as a dashed red line that merges, at $M > 1\ M_\odot$, in the solid red line corresponding to the prestellar component, suggesting that all the cores more massive than the solar mass are prestellar. Considering Poissonian uncertainties and varying the bin size within reasonable limits (10% around a bin size = 0.2), we obtain for masses $M > 1\ M_\odot$ a slope of -0.76 ± 0.51, where the uncertainty is dominated by the poor statistics. Even if this value is lower than that found in the Vela-C molecular cloud by Giannini et al. (2012) and in the outer Galaxy by Elia et al. (2013), given the large uncertainty involved, we cannot claim meaningful differences.

In the same figure we also show (bottom panel) the $L_{\rm bol}$ versus $M_{\rm env}$ diagram for the VMR-D protostars with the evolutionary tracks computed by Molinari et al. (2008) for different initial envelope masses superimposed. For comparison we also report the starless sources, noting that they populate the low-luminosity

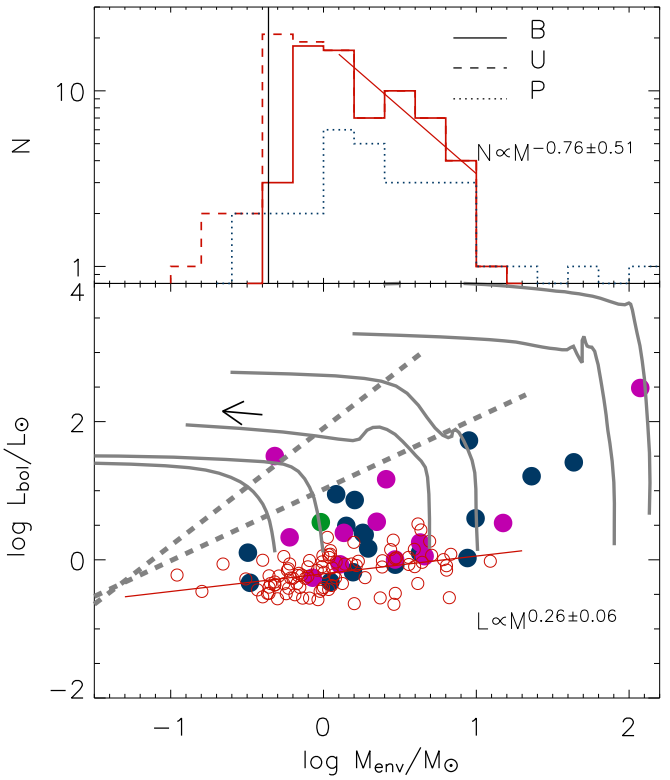

Figure 12. Upper panel: mass distribution for starless and protostellar *Herschel* sources detected ON-cloud. The red lines refer to the starless sources that are subdivided into unbound (dashed) and bound (solid) cases. The dotted blue line indicates the protostellar sources of Table 6, while the vertical solid line is the completeness limit implied by the photometry limits in Table 1. Lower panel: $L_{\rm bol}$ vs. $M_{\rm env}$ diagram: filled and open circles represent protostars and starless cores, respectively. Protostars classified as Class 0, I, and FS in Table 4 are indicated with blue, magenta, and green filled circles, respectively. The superimposed gray lines represent the evolutionary tracks computed for different initial envelope masses by Molinari et al. (2008) to follow the path of a protostar in this diagram. The rising part corresponds to the main accretion phase ending with the transition region between Class 0 and Class I objects. This region is delimited by the two dashed lines taken from André et al. (2000) that ideally separate objects with $M_{\rm env} > M_\star$ (lower) from those with $M_{\rm env} < M_\star$ (upper). The arrow shows the evolutionary direction, and the red straight line is a linear fit to the starless sources.

part of the diagram and show a relatively smaller luminosity spread with respect to the protostars. A linear fit to their distribution in this diagram gives a slope that is shallower than that found in both Vela-C (Giannini et al. 2012) and the third Galactic quadrant (Elia et al. 2013), suggesting possible differences in the clump/core-forming mechanism. On the other hand, the protostars are more widely distributed in this diagram, with most of them being located on the rising branch of the evolutionary tracks corresponding to the main accretion phase. Following André et al. (2000), we also report in this diagram two lines that delimit what is thought to be the transition zone separating the low-luminosity branch in which $M_{\rm env} > M_\star$, generally associated with the Class 0 phase, from the region in which $M_{\rm env} < M_\star$, corresponding to the Class I and later phases. Remarkably, in most cases the protostars fall below the transition region, suggesting a very recent SF episode. However, a similar distribution of the protostars is also seen in other SFRs observed with *Herschel* (Giannini et al. 2012; Elia et al. 2013), and this seems to be unrealistic, raising a problem of consistency with the model. From an observational point of view, one possibility is that as a result of our need to know at least three fluxes at $\lambda \geqslant 160\,\mu$m to appropriately fit a modified blackbody, we introduce a selection effect favoring the earliest objects, a point that should be better considered in future work.

7. CONCLUSIONS

In this work we have studied the YSO population in the VMR-D cloud by exploiting both the *Spitzer*-PSC catalog, obtained from *Spitzer* observations and published in Paper I, and the recent *Herschel* observations carried out during the completion of the Hi-GAL key program involving part of this region. The main results can be summarized as follows.

1. A list of 1470 candidate YSOs, identified out of the ∼170,000 *Spitzer*-PSC catalog sources, has been obtained through a selection pipeline designed to exclude reddened normal stars, as well as Galactic and extragalactic contaminants.
2. YSOs have been subdivided into classes according to their spectral slope in the near-/mid-IR and their relative numbers (86, 53, 136, and 282 for Class I, FS, II, and III, respectively), obtained after subtraction of the estimated background population, have been compared with those characterizing other star-forming clouds showing that the YSO content in VMR-D is similar to that seen in Ophiuchus and in the western part of Perseus.
3. The *Spitzer*-PSC catalog has been complemented to obtain the largest data set on the continuum spectrum of the sources, including fluxes from the 2MASS and *WISE* public surveys, as well as from new *Herschel* FIR observations and previous 1.2 mm SEST-SIMBA continuum mapping of the VMR-D region.
4. The *Herschel*/Hi-GAL maps ($\lambda = 70, 160, 250, 350,$ and $500\,\mu$m) overlapping our VMR-D region have been first used to identify the ON-cloud regions delimited by a column density $N(\mathrm{H_2}) = 6.5 \times 10^{21}$ cm^{-2} and then analyzed to obtain a merged catalog of compact FIR sources useful for searching additional protostars undetected by *Spitzer*. This catalog, complemented with fluxes coming from the *Spitzer*-PSC catalog, as well as from *WISE* and the 1.2 mm catalog, has been exploited to find and characterize 30 protostellar and 92 starless sources and to evaluate their bolometric luminosities and temperatures.
5. Bolometric luminosities and temperatures have also been obtained for 33 *Spitzer*-selected ON-cloud protostars. These have been plotted in an $L_{\rm bol}$ versus $T_{\rm bol}$ diagram showing that 7 (6 Class I, and 1 FS) out of these 33 protostars can actually represent Class 0 objects as a result of their low bolometric temperature ($T_{\rm bol} < 70$ K).
6. The distributions of the luminosities of both the *Spitzer*- and *Herschel*-selected protostars show a bright outlier, corresponding to the same object, *Spitzer*-PSC 42629 (IRS17 in Liseau et al. 1992), suggesting that VMR-D is also forming relatively high mass objects.
7. The complete PLF of the ON-cloud region covered by both *Spitzer* and *Herschel* observations has been obtained by merging together the 33 *Spitzer*-selected and the 30 *Herschel*-selected protostars. Given that 10 objects are in both samples, we count a total of 53 objects and find that *Spitzer* is able to detect approximately two-thirds of the protostellar population actually present in VMR-D. This stresses the need for using also the *Herschel* observations in studying the earlier protostellar phases.
8. The envelope masses have been obtained for all the *Herschel* protostellar sources detected ON-cloud and for which

an envelope temperature can be determined. A plot of the masses versus the corresponding luminosities shows that by comparison with evolutionary tracks, we are mainly sampling objects in the main accretion phase. A possibility is that a selection effect is implied by our preference for sources also detected in the FIR, a choice that is dictated by the need to obtain accurate bolometric quantities.

REFERENCES

André, P., Ward-Thompson, D., & Barsony, M. 1993, ApJ, 406, 122
André, P., Ward-Thompson, D., & Barsony, M. 2000, in Protostars and Planets IV, ed. V. Mannings, A. P. Boss, & S. S. Russell (Tucson, AZ: Univ. Arizona Press), 59
Bernard, J. P., Paradis, D., Marshall, D. J., et al. 2010, A&A, 518, L88
Budavári, T., & Szalay, A. S. 2008, ApJ, 679, 301
Cambrésy, L. 1999, A&A, 345, 965
Chen, H., Myers, P. C., Ladd, E. F., & Wood, D. O. S. 1995, ApJ, 445, 377
Cutri, R. M., Wright, E. L., Conrow, T., et al. 2013, http://wise2.ipac.caltech.edu/docs/release/allwise/expsup/index.html
Dunham, M. M., Harce, H. G., Allen, L. E., et al. 2013, AJ, 145, 94
Dunham, M. M., Stutz, A. M., Allen, L. E., et al. 2014, in Protostars and Planets VI, ed. H. Beuther, R. Klessen, C. Dullemond, & Th. Henning (Tucson, AZ: Univ. Arizona Press)
Elia, D., Massi, F., Strafella, F., et al. 2007, ApJ, 655, 316
Elia, D., Molinari, S., Fukui, Y., et al. 2013, ApJ, 772, 45
Evans, N. J., II, Dunham, M. M., Jørgensen, J. K., et al. 2009, ApJS, 181, 321
Flaherty, K. M., Pipher, L. J., Megeath, S. T., et al. 2007, ApJ, 663, 1069
Froebrich, D., & Rowles, J. 2010, MNRAS, 406, 1350
Giannini, T., Elia, D., Lorenzetti, D., et al. 2012, A&A, 539, A156
Giannini, T., Lorenzetti, D., De Luca, M., et al. 2013, ApJ, 767, 147
Giannini, T., Massi, F., Podio, L., et al. 2005, A&A, 433, 941
Gutermuth, R. A., Megeath, S. T., Myers, P. C., et al. 2009, ApJ, 184, 18
Harvey, P., Merin, B., Huard, T. L., et al. 2007, ApJ, 663, 1149
Harvey, P. M., Chapman, N., Lai, S., et al. 2006, ApJ, 644, 307
Harvey, P. M., Huard, T. L., Jørgensen, J. K., et al. 2008, ApJ, 680, 495
Hildebrand, R. H. 1983, QJRAS, 24, 267
Hsieh, T.-H., & Lai, S.-P. 2013, ApJS, 205, 5
Joshi, Y. C. 2005, MNRAS, 362, 1259
Kirk, J. M., Ward-Thompson, D., Di Francesco, J., et al. 2009, ApJS, 185, 198
Kryukova, E., Megeath, S. T., Gutermuth, R. A., et al. 2012, AJ, 144, 31
Lada, C. J. 1987, in IAU Symp. 115, Star Forming Regions, ed. M. Peimbert & J. Jugaku (Dordrecht: Reidel), 1
Lada, C. J., Lombardi, M., Roman-Zuniga, C., et al. 2013, ApJ, 778, 133
Liseau, R., Lorenzetti, D., Nisini, B., et al. 1992, A&A, 265, 577
Lombardi, M., Lada, C. J., & Alves, J. 2013, A&A, 559, A90
Lorenzetti, D., Giannini, T., Vitali, F., et al. 2002, ApJ, 564, 839
Markwardt, C. B. 2009, in ASP Conf. Ser. 411, Astronomical Data Analysis Software and Systems XVIII, ed. D. A. Bohlender, D. Durand, & P. Dowler (San Francisco, CA: ASP), 251
Massi, F., De Luca, M., Elia, D., et al. 2007, A&A, 466, 1013
Massi, F., Lorenzetti, D., Giannini, T., et al. 2000, A&A, 353, 598
Molinari, S., Pezzuto, S., Cesaroni, R., et al. 2008, A&A, 481, 345
Molinari, S., Schisano, E., Faustini, F., et al. 2011, A&A, 530, A133
Molinari, S., Swinyard, B., Bally, J., et al. 2010, PASP, 122, 314
Motte, F., & André, P. 2001, A&A, 365, 440
Murphy, D. C., & May, J. 1991, A&A, 247, 202
Myers, P. C., Adams, F. C., Chen, H., et al. 1998, ApJ, 492, 703
Myers, P. C., & Ladd, E. F. 1993, ApJL, 413, L47
Offner, S. S. R., & McKee, C. F. 2011, ApJ, 736, 53
Olmi, L., Ade, P. A. R., Anglés-Alcazar, D., et al. 2009, ApJ, 707, 1836
Pascale, E., Ade, P. A. R., Bock, J. J., et al. 2008, ApJ, 681, 400
Pezzuto, S., Elia, D., Schisano, E., et al. 2012, A&A, 547, A54
Piazzo, L., Ikhenaode, D., Natoli, P., et al. 2012, ITIP, 21, 3687
Roseboom, I. G., Oliver, S., Parkinson, D., et al. 2009, MNRAS, 400, 1062
Shu, F. H. 1977, ApJ, 214, 488
Skrutskie, M. F., Cutri, R. M., Stiening, R., et al. 2006, AJ, 131, 1163
Strafella, F., Elia, D., Campeggio, L., et al. 2010, ApJ, 719, 9
Stutz, A. M., Tobin, J. J., Stanke, T., et al. 2013, ApJ, 767, 36
Suutarinen, A., Haikala, L. K., Harju, J., et al. 2013, A&A, 555, A140
Winston, E., Bourke, T. L., Megeath, S. T., et al. 2011, ApJ, 743, 166
Wouterloot, J. G. A., & Brand, J. 1999, A&AS, 140, 177
Young, C. H., & Evans, N. J. 2005, ApJ, 627, 293